Surfaces and Interfaces 72 (2025) 107016

Contents lists available at ScienceDirect

Surfaces and Interfaces

journal homepage: www.sciencedirect.com/journal/surfaces-and-interfaces

Anti-icing performance and anti-corrosive properties of superhydrophobic nanosecond-laser-textured aluminum surfaces with a self-assembled monolayer coating

Matic Može [a,*], Peter Rodič [b], Tim Štrus [a], Miha Štucin [a], Yuheng Shang [c], Robert Lovšin [a], Nina Kovač [b], Samo Jereb [a], Armin Hadžić [a], Matevž Zupančič [a], Maria Rosaria Vetrano [c], Iztok Golobič [a]

[a] University of Ljubljana, Faculty of Mechanical Engineering, Aškerčeva c. 6, SI-1000 Ljubljana, Slovenia
[b] Jožef Stefan Institute, Department of Physical and Organic Chemistry, Jamova c. 39, SI-1000 Ljubljana, Slovenia
[c] KU Leuven, Department of Mechanical Engineering, Division of Applied Mechanics and Energy Conversion (TME), B-3001 Leuven, Belgium

ARTICLE INFO

Keywords:
Superhydrophobic surfaces
Freezing delay
Icephobic surfaces
Laser-textured surfaces
Corrosion protection
Aluminum

ABSTRACT

Water and ice accumulation on surfaces present significant challenges in numerous fields, causing issues such as corrosion of metallic surfaces and a broad range of problems associated with increased weight, altered hydro-/aerodynamics, vibrations, and heat transfer resistance. Currently, passive solutions, such as functionalized surfaces that also offer improved anti-corrosive properties, are being focused on. This study presents the fabrication and evaluation of four functionalized superhydrophobic surfaces on 1050A aluminum alloy samples using nanosecond laser texturing and self-assembled monolayer grafting to enhance anti-icing and corrosion protection. The developed surfaces exhibited superhydrophobicity with static and dynamic contact angles above 163° and a contact angle hysteresis below 2°, maintaining their nonwetting properties after multiple icing/deicing cycles. Three surfaces significantly lowered ice nucleation temperature with the lowest average value of -20.1 °C recorded on the surface with shallow, non-distinct features. The freezing delay was prolonged up to 468 % and 944 % at -15 °C and -20 °C, respectively, in comparison with the untreated reference surface. The superior anti-icing properties of the two surfaces with shallow structures, fabricated using a lower laser pulse fluence than those with deep structures, are ascribed to a lower number of potential active nucleation sites for condensation of water vapor and freezing initiation. In comparison with an untreated surface, ice adhesion was reduced by up to 60 % on surfaces with shallow features but increased between 33 % and 84 % on surfaces with deep morphological features. Repeatable cascade freezing was observed on one of the surfaces, which also exhibited the poorest anti-icing performance. Surfaces with non-distinct or irregular channels exhibited better corrosion properties than surfaces featuring well-defined laser-etched channels. The surface with the lowest surface roughness exhibited the best properties in all evaluations, providing a good starting point for future optimization with a focus on surfaces with micron scale and submicron features instead of the more traditional surfaces with structures on the scale of tens of microns. Overall, this functionalization approach is promising for industrial use, simultaneously offering enhanced robustness, anti-icing behavior, and corrosion protection.

1. Introduction

Water and ice accumulation on surfaces pose significant challenges in many fields. Prolonged contact with water can degrade most metallic surfaces due to corrosion, leading to a loss of function and shortened lifespan. Ice accumulation causes a broad range of problems, including increased weight, changes in aerodynamic/hydrodynamic properties, vibrations, and heat transfer resistance. Icing and frosting are particularly problematic in aviation, power transmission lines, wind turbines, maritime transport, and heat exchangers such as heat pump evaporators [1–3]. Ice accumulation is typically prevented by heating the susceptible surface, while accumulated ice may be removed by flexible (inflatable)

* Corresponding author.
E-mail address: matic.moze@fs.uni-lj.si (M. Može).

https://doi.org/10.1016/j.surfin.2025.107016
Received 2 October 2024; Received in revised form 4 June 2025; Accepted 19 June 2025
Available online 20 June 2025

surfaces, heating, deicing sprays, vibration, or simple mechanical force. These active methods mostly require energy input and management systems, necessitating the development of passive alternatives such as functionalized surfaces to prevent ice formation and accumulation. In many cases, icephobic surfaces also possess improved anti-corrosive properties [4–7]. Functionalized surfaces are therefore promising especially in scenarios such as aircraft components, offshore platforms, or wind turbine blades, where both anti-icing and corrosion resistance are critically needed.

Different approaches may be used to impart icephobic properties to surfaces, including surface coatings and hydrated or slippery surface layers. The state-of-the-art surface engineering strategies mostly aim to influence the solid-liquid-vapor interaction. The strategies include the fabrication of both dry and wet (*i.e.*, lubricated) surfaces, with various chemical functionalities and length scales. Smooth surfaces with or without coatings offer easy application and simplicity of their design [8]. Although the lack of micro/nanostructures can make them more robust, roughness tends to develop through corrosion and exposure to the environment, hindering their ice and frost repellency over time [9]. Surfaces incorporating hydrophobic lubricating layers (SLIPS) have shown very promising results [10,11], yet the expectations of their practicality are hampered by concerns regarding their currently limited longevity due to oil depletion. Textured surfaces with microstructures [12–14] or nanostructures [15,16] have arguably received the most research attention of all. Surface micro/nanostructures have been shown to critically influence where and under what conditions freezing occurs. However, without low-surface-energy coatings to further augment their interaction with both water and ice and increase their durability, they fail to fulfill most criteria of an ideal functionalized icephobic surface. One preferred solution is the use of hierarchical surfaces with a combination of microscale and nanoscale features, possibly supplemented by millimetric-scale macrostructure [17,18].

Regardless of the exact approach to surface functionalization, the goal is to provide a multifaceted strategy for combating icing on cold surfaces. Firstly, prolonged contact of water with the surface may be prevented by imparting water repellency and shedding of water droplets. However, it is reasonable to expect that some droplets will inevitably stay on the surface long enough to freeze. Therefore, delaying the start of freezing and decreasing the ice nucleation temperature is preferable. If the water on the surface eventually freezes, the ice adhesion should be low to allow for easy removal of the ice layer. If a surface can be made to exhibit all these properties, it represents a comprehensive strategy against ice accumulation.

Various state-of-the-art surface functionalization approaches have been demonstrated to date in the field of icephobic surface engineering, including electrochemical treatments [19], lithography [20], etching [21–24], template methods [25], and spray coating [26]. For example, Yu et al. [27] used hot pressing to form micro-/nanostructures on a polypropylene with candle soot, forming a superhydrophobic engineered surface with photothermal electrical conversion capabilities, capable of delaying freezing of water droplets and reducing ice adhesion.

Among the available techniques, laser micromachining [28,29] offers simplicity, flexibility, and speed at an affordable cost, all while being able to produce extremely varied surface micro/nanostructures, which have been demonstrated to favorably mitigate icing when combined with appropriate coatings [30–33]. Furthermore, laser texturing has been used to prepare (super)hydrophobic surfaces for corrosion prevention [34–39], phase-change heat transfer enhancement [40–43], self-cleaning properties [44–49], and friction reduction [50–55]. Wang et al. [56] employed laser etching to construct micropillar arrays on a photothermally responsive shape memory polymer and evaluated the passive anti-icing and active deicing performance characteristics of the functionalized surfaces. Compared to a smooth hydrophobic surface, the onset of freezing was delayed by 221 % at −20 °C on the best-performing surface. Vercillo et al. [57] investigated ice adhesion strength and the chemical stability of metal alloys (AA2024 and Ti64) textured with a UV nanosecond laser via direct laser writing (DLW). The results showed that the ice adhesion was not reduced and the superhydrophobicity resulting from the one-step laser treatment was lost after 16 consecutive icing and deicing cycles. The authors attribute the loss of superhydrophobicity to the fragility of the non-polar carbon layer adsorbed on the surface. Alamri et al. [31] explored direct laser interference patterning (DLIP) of titanium airfoils and evaluated the anti-icing performance of the laser-treated airfoil in an icing wind tunnel under simulated atmospheric conditions. Self-limiting ice growth was observed together with a decrease in the deicing electro-thermal power up to 80 %, and up to 60 % lower heating power necessary to keep the surface free of ice compared to the reference airfoil. Rico et al. [58] performed a systematic study of the wetting and freezing properties of 6061 aluminum alloy, which they subjected to nanosecond pulsed IR laser treatments to modify its surface roughness and morphology. Plasma-enhanced chemical vapor deposition (PECVD) was used to apply a thin CF_x layer onto the surface to reduce its free energy and render it superhydrophobic. Surface morphology rather than the actual value of the surface roughness was shown to be the key feature ensuring a long delay of heterogeneous nucleation. Volpe et al. [59] used femtosecond laser texturing to produce superhydrophobic surfaces with anti-icing properties on 2024 aluminum alloy. The textured substrates presented self-cleaning properties and robust water repellency with water droplets bouncing off the tilted surfaces even at −20 °C. Wang et al. [60] fabricated microstructured flexible films using laser processing and functional nanocomposites. The electrothermal and photothermal response of the film allowed it to maintain its superhydrophobicity even at temperatures as low as -30 °C. Finally, Wang et al. [61] summarized the recent developments in the field of ultrafast laser-fabricated superhydrophobic anti-icing surfaces, showcasing many unique micro-nanostructures developed and reported in the literature. They critically point out three common shortcomings of such surfaces: Cassie–Baxter stability, surface durability, and environmental adaptivity.

In addition to ice nucleation temperature reduction and freezing delay increase, ice adhesion strength is commonly focused on in the development of functionalized icephobic surfaces. In this field, Milles et al. [62] investigated the variation of the ice adhesion strength of DLIP and DLW laser-textured 2024 aluminum alloy surfaces, and have shown that optimum surface textures lead to a reduction of the ice adhesion strength from the original values of 57 kPa to just 6 kPa. Zheng et al. [63] fabricated micro-groove structures on Ti6Al4V substrates direct laser interference lithography (DLIL), coating them with lubricant oil to obtain a hybrid surface with the oil firmly locked and stored in the groove structures. This allowed the oil to be self-supplemented even after 10 icing/deicing cycles, leading to an efficient anti-icing performance as well as improved durability and robustness with the apparent contact angle (CA) of 143° and ice adhesion strength of 7.16 kPa. Boinovich et al. [64] investigated the ice adhesion on superhydrophobic and SLIPS surfaces and confirmed a strong temperature dependence of the adhesion strength. Laser-fabricated superhydrophobic surfaces exhibited higher adhesion strength in comparison with the SLIPS surfaces but better resisted degradation after multiple test cycles. Liu et al. [65] prepared both hydrophilic and hydrophobic laser-textured samples on nickel samples and investigated ice adhesion strength under the presence of frosting before the formation of the test ice sample in a mold. The results show that the presence of frost significantly increases the adhesion strength of ice, which the superhydrophobic laser-fabricated surface otherwise successfully decreased by an order of magnitude in comparison with a reference surface. Liu et al. [66] investigated the anisotropic ice adhesion of groove-shaped femtosecond-laser-made textures on A6061-T6 aluminum alloy and found that the ice adhesion strength is notably smaller when tested parallel to the laser-made grooves than perpendicularly to the groove direction.

In addition to using laser-texturing solely for imparting the surface with anti-icing properties, several studies investigated the concomitant

enhancement of corrosion protection, mainly stemming from the superhydrophobic behavior of most surfaces [48]. Montes et al. [67] report a procedure for the functionalization of stainless steel surfaces, consisting of surface nanostructuring through laser treatment and electron beam evaporation followed by infiltration of a fluorine coating liquid. The fabricated surfaces provide superhydrophobicity, omniphobicity (*i.e.*, repellency towards all liquids regardless of their surface tension), self-cleaning, anti-fouling, and effective anti-icing capacity, while still exhibiting favorable corrosion resistance. Li et al. [68] prepared a superhydrophobic surface on carbon steel via a simple and fluorine-free method, *i.e.*, multiple-pulse laser ablation followed by chemical modification with hexadecyltrimethoxysilane. The surface exhibited favorable photothermal properties, significantly lower corrosion current density, delayed ice nucleation, and lower deicing force compared to an untreated surface. Cui et al. [69] constructed hierarchical micro-/nanostructures on a Zr-based metallic-glass surface using nanosecond laser ablation and rendered the surface superhydrophobic via a subsequent heat treatment in air. In comparison with an untreated reference, the superhydrophobic surface increased the corrosion resistance and freezing time while also decreasing the freezing temperature. Shu et al. [70] utilized nanosecond laser processing and sol-gel coating to fabricate a mechanically robust micro-/nanostructured coating on copper substrate. The produced superhydrophobic surfaces exhibited favorable properties such as self-cleaning, wear resistance, anti-icing, and enhanced corrosion resistance.

An abundance of methods is available to impart surfaces (especially metallic ones) with superhydrophobic properties, for which an appropriate combination of micro-/nanostructures and surface chemistry is required. While significant achievements in terms of separately realizing anti-icing and anti-corrosive properties have been presented to date, few studies apply a rational approach in terms of varying the surface morphology to investigate how it impacts the behavior of functionalized surfaces in corrosive and icing environments. Random surface microstructures are commonly fabricated, making it difficult to compare different treatment parameters and pin down mechanisms behind superior (or inferior) anti-icing and anti-corrosive properties. Our work takes a more comprehensive approach by assessing both the anti-icing and anti-corrosion properties of purposely created laser-induced microstructures. This dual evaluation of anti-icing and corrosion resistance is rarely explored in the literature despite being crucial for practical applications, where a superhydrophobic surface should fulfill both functions. We not only examine the effect of different laser processing conditions on wettability but also systematically analyze how variations in surface morphology influence ice nucleation, ice adhesion, and corrosion resistance. Furthermore, the presented surface fabrication approach is scalable, flexible, and fast, making it suitable for industrial implementation.

Specifically, this study investigated the anti-icing and anti-corrosive properties of superhydrophobic laser-textured aluminum surfaces. The substrates made of 1050A aluminum alloy are first laser-textured using a nanosecond pulsed laser to produce four variations with different depths and spacing of the laser-made microchannels. In the second step, the surfaces are hydrophobized with a self-assembled monolayer of fluoroalkyl phosphonic acid. Profilometric, SEM, and EDS analyses are performed. Dynamic contact angles and degradation during multiple freezing/thawing cycles are evaluated. Anti-icing properties of the functionalized surfaces are evaluated by recording the nucleation temperature of sessile droplets and by observing the temporal delay until nucleation at a given (subzero) temperature. Ice adhesion was evaluated by determining the shear force necessary to remove a $20 \times 20 \times 20$ mm^3 ice cube from the surface at -20 °C. Finally, the corrosion resistance is evaluated in a 0.1 M NaCl solution through potentiodynamic polarization measurements.

2. Materials and methods

2.1. Surface preparation and analysis

The procedure outlined in Fig. 1 was employed to prepare the functionalized surfaces. Briefly, the samples were ultrasonically cleaned, laser textured, ultrasonically cleaned again, cleaned using UV/ozone treatment, hydrophobized by drop casting, and dried. Detailed descriptions of the surface treatment steps are given below.

Functionalized surfaces were fabricated on 1 mm thick 38×38 mm^2 alumnum plates (1050A H24, >99.5 % Al). Before laser texturing, the aluminum substrates were ultrasonically cleaned in acetone, ethanol, and distilled water for 15 min (in each medium).

Laser texturing was performed using a nanosecond fiber laser (JPT Opto-electronics Co., Ltd., M7 30 W MOPA; $\lambda = 1064$ nm). The laser beam was focused onto the surface using an F-Theta lens with a 70×70 mm working area and a 100 mm focal length. The focused beam had an approximate diameter of 25 μm, with a manufacturer-reported laser beam quality of $M^2 < 1.3$ and a maximum laser source power of 30 W. The surfaces were prepared using a scanning pattern of parallel lines with a spacing of Δx between the consecutive lines. Four combinations of laser texturing parameters were used to prepare four surfaces with different surface properties. The employed parameters are summarized in Table 1, where t_p denotes the duration of the laser pulse, P the average power of the laser, v the scanning speed, f the pulse frequency, Δx the lateral distance between the consecutive scanning lines, δ the distance between the locations of the centers of two consecutive laser pulses, and F the average fluence of the laser. The letter in the name of each sample denotes the depth of the produced laser-etched channels (S = shallow, D = deep) and the number indicates the lateral spacing of the scanning lines in micrometers.

After laser texturing, the samples were further cleaned for 15 min in isopropanol using an ultrasonic bath, with the textured side facing downward to aid the removal of debris and loosely attached particles. Subsequently, the samples were placed in a UV/ozone cleaner (Ossila) for 15 min to remove adsorbed contaminants and prepare the surface for grafting with a hydrophobization agent. Following this second cleaning step, the surfaces were hydrophobized using a 1 mM solution of 3,3,4,4,5,5,6,6,7,7,8,8,9,9,10,10,11,11,12,12,12-henicosafluorododecylphosphonic acid (abbreviated to FDPA, CAS No. 252237–39–1, abcr GmbH) dissolved in 2-propanol (Honeywell, ACS reagent, ≥99.5 %). The FDPA solution was pipetted onto the samples to completely cover their surface and was subsequently left to dry for fifteen minutes at room temperature before being placed in an oven at 120 °C for 60 min to finalize drying and strengthen the bond to the surface. FDPA has been previously used for lowering the free surface energy and achieving (super)hydrophobicity in multiple existing literature works [29,43,71–78], where immersion coating, dip coating or drop casting were used to apply a FDPA monolayer to a range of different materials, including alumina, ITO, different aluminum alloys and copper.

Two additional surfaces were prepared as baselines for comparing enhanced anti-icing properties and improved corrosion protection. Firstly, an untreated surface “REF” was prepared with no treatments other than the first cleaning step shown in Fig. 1. Secondly, a hydrophobized but otherwise untreated surface “REF-H” was prepared by applying all steps shown in Fig. 1 except for laser texturing.

Surface wettability was analyzed by measuring the apparent static and dynamic contact angles. The apparent static contact angles were measured using an Ossila contact angle goniometer (Ossila LTD, with high-resolution 1920 × 1080 camera, measurement range between measurement range between 5° and 180°, accuracy ±1°) at room ambient temperature, while the dynamic contact angles were evaluated using a custom-made experimental setup, also at room temperature. The surface morphology was assessed utilizing a scanning electron microscope (Helios Nanolab 650 FEI). Imaging was performed by SEM using secondary electron imaging (SEI) mode at 5 kV energy. The surface

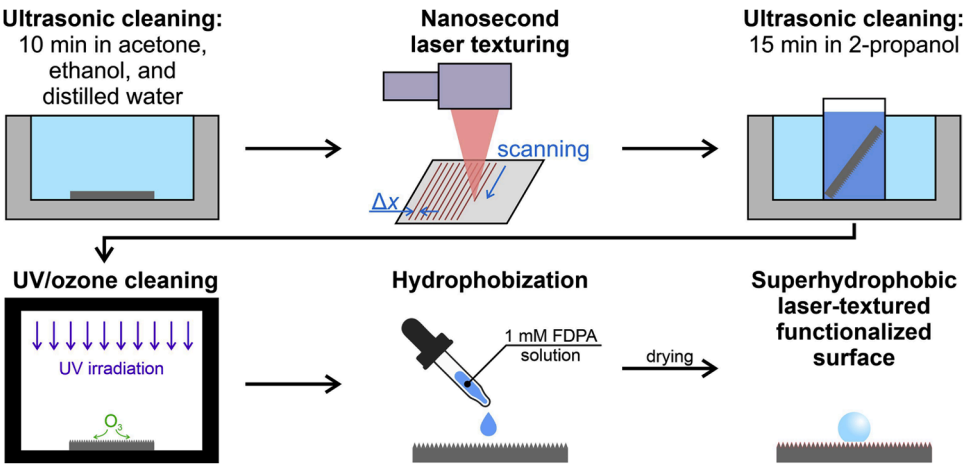

Fig. 1. Surface functionalization procedure.

Table 1
Laser-texturing parameters used to treat the samples in this study.

Sample	t_p (ns)	P (W)	v (mm s^{-1})	f (kHz)	Δx (μm)	δ (μm)	F (J cm^{-2})
S-25	45	18	1650	110	25	15	33.3
S-50	45	18	1650	110	50	15	
D-25	100	18	400	80	25	5	45.8
D-50	100	18	400	80	50	5	

composition analysis of the selected areas was obtained using energy-dispersive X-ray spectroscopy (EDS Aztec software) at 5 kV energy. EDS collected the signal for at least 60 s and the representative values were presented. The surface roughness of the samples was evaluated using a digital microscope (Keyence VHX-6000). The surface 3D topography of the untreated treated aluminum was evaluated at three randomly selected spots using a stylus contact profilometer (Bruker DektakXT model). The device featured a 2 μm tip and operated in soft-touch mode with a force of 1 mN. Measurements were conducted over an area of 0.75 mm × 0.75 mm, with a vertical analysis range of 65.5 μm and a vertical resolution of 0.167 μm/point. The data collected were analyzed using TalyMap Gold 6.2 software. The results are displayed as 3D images, with the corresponding surface roughness (Sa) presented as average values ± standard deviations.

The chemical composition of the aluminum surface and FDPA (powder; used as a reference), as well as that of the laser-structured surface (DT50, DT25, ST50 and ST25) with and without FDPA coating, was analyzed using universal attenuated total reflectance Fourier transform infrared (ATR-FTIR) spectroscopy (Bruker ALPHA II). The spectra, recorded in transmittance mode, were collected over the range of 4000 to 500 cm^{-1} with a resolution of 4 cm^{-1} by averaging four scans. In the manuscript, the spectra are presented in the range between 1600 and 600 cm^{-1}, where characteristic bands for FDPA molecules were observed (phosphate anchor head and perfluoro tail).

2.2. Experimental setups for evaluation of anti-icing properties

Measurements of ice nucleation temperature, freezing delay, and observation of the freezing process were conducted using a custom-made experimental setup, as depicted schematically in Fig. 2(a). Individual samples were placed on a thermoelectric ("Peltier") element, which was powered by a PID controller (Meerstetter TEC-1123-HV) and controlled via the controller's proprietary TEC Service Software. A type K thermocouple was installed to monitor the temperature of the sample's surface. Heat dissipation from the warm side of the thermoelectric element was realized using a water-cooling block within a closed cooling loop, connected to a pump and a radiator. An acrylic transparent chamber was mounted on top of the water-cooling block, in which the temperature and the relative humidity were monitored using the SparkFun SHTC3 (Qwiic) sensor and the SparkFun RedBoard Qwiic Arduino board. The humidity within the chamber was kept low by using 4 Å molecular sieves (relative humidity < 10 %) or silica gel (relative humidity 15-20 %). The freezing processes were monitored and recorded using a USB camera (IDS UI-3080CP-C-HQ Rev.2).

Ice adhesion strength was determined using a custom-designed setup shown schematically in Fig. 2(b). The setup is based around a motorized test stand (Axis STAH500/300) equipped with a push/pull force sensor (Axis FC200). The same cooling subassembly is used as on the setup for freezing delay and ice nucleation temperature measurement, including the water cooling block, a closed cooling system and a 2-stage TEC cooler. The plunger of the force sensor is equipped with a 3D-printed attachment to limit heat transfer from the ice cube and provide a large contact area close to the droplet's base, limiting the formation of a secondary tension/compression field under the ice cube and ensuring that shearing is the predominant method of loading [79]. The distance between the bottom of the plunger's adapter and the surface was < 1 mm.

2.3. Evaluation of the ice nucleation, freezing time delay, and the freezing process

To evaluate the ice nucleation temperature, 15 water droplets ($V = 7$ μL) were placed on the surface at room temperature. Ice nucleation measurements were initiated once the surface was cooled down to 5 °C using the thermoelectric element. During each measurement, a cooling rate of 0.1 K s^{-1} was maintained using the PID controller. During the measurement, freezing of the droplets was recorded with the camera in a top-down orientation. Droplet evaporation was found to be negligible during the measurements. The measurement was concluded when all droplets on the surface had frozen, after which the surface was brought back to room temperature. This procedure was repeated with the same set of droplets to obtain a second set of ice nucleation measurements. Subsequently, a new set of droplets was placed, and two additional sets of ice nucleation measurements were conducted, resulting in four sets of ice nucleation measurements per surface. The entire evaluation was conducted at two relative humidity levels, namely at 15–20 % using the silica gel as the desiccant and at <10 % using molecular sieves as the desiccant. To extract the ice nucleation temperature, the camera recording was manually synchronized with the recorded sample temperatures. Ice nucleation was easily observable in the recordings as a sudden change in droplet appearance with a transition from transparency to an opaque (white) color. Based on the accuracy of the

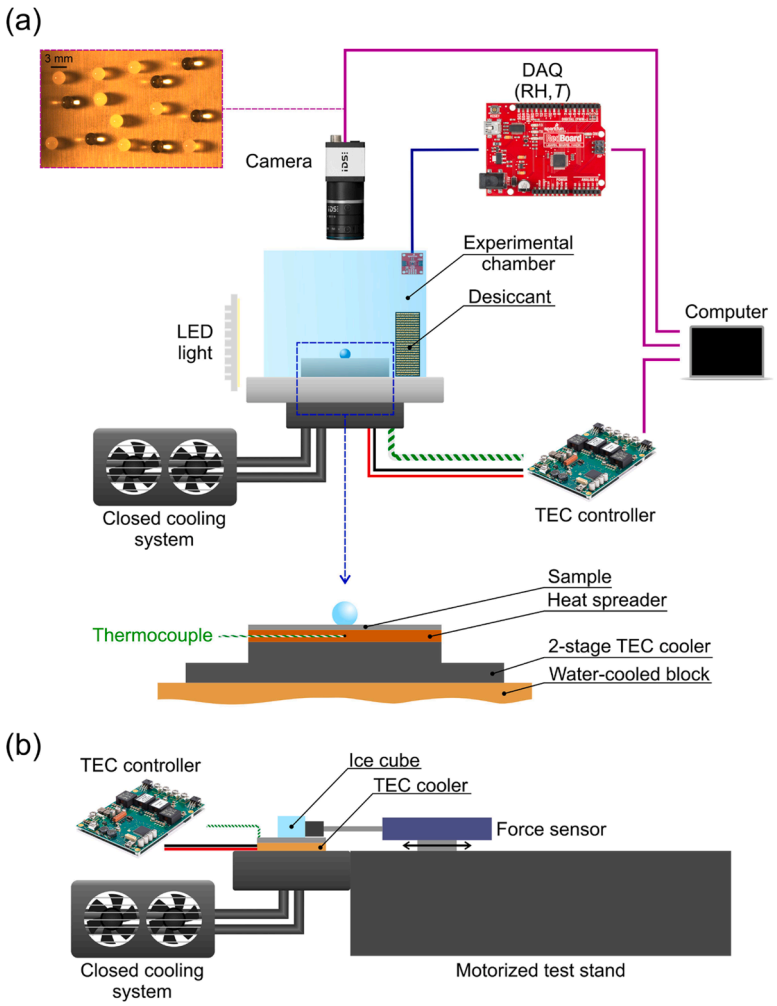

Fig. 2. Schematic of the custom-made experimental setup used for the evaluation of (a) freezing delay and nucleation temperature and (b) ice adhesion strength.

temperature sensor and the synchronization between the recording and the temperature data, we estimate the accuracy of the nucleation temperature to be approx. ± 0.3 K.

The freezing delay of water droplets was evaluated in a similar manner. Fifteen water droplets ($V = 7$ μL) were placed on the samples at room temperature and silica gel was used as the desiccant. Measurements were performed by cooling the surface at a cooling rate of 1 K s^{-1} to a target temperature of either −15 °C, −17.5 °C, or −20 °C. The freezing process was again recorded using a camera from a top-down perspective. Two sets of measurements were performed on each surface for each target temperature. The freezing delay was measured from the moment the cooling started. It should be noted that in some cases (especially at the lowest target temperatures) individual droplets froze before the target temperature was reached, which was also logged. The accuracy of determination of the freezing delay is approx. 2 s.

Finally, the freezing process was visualized on selected surfaces to compare their behavior. A 7 μL water droplet was placed on the sample at room temperature, and low relative humidity inside the chamber was maintained using silica gel. During this measurement, the sample was cooled at a cooling rate of 0.5 K s^{-1} while the droplet was recorded from a side-view perspective. Post-processing of all recorded data was carried out using MathWorks MATLAB R2021b and R2022b.

2.4. Evaluation of ice adhesion strength

Ice adhesion strength was evaluated on all functionalized and reference surfaces using the following methodology. Firstly, an ice cube was formed on the surface by placing a silicone mold with inner dimensions of 20 × 20 × 20 mm^3 onto the surface at room temperature and filling it with double-distilled water. Then, the TEC cooler was used to cool the surface to −20 °C to freeze the water in the mold to form the ice cube. When the solidification of the cube was complete, the mold was removed and the motorized test stand bearing the force sensor was moved towards the ice cube at 10 mm min^{-1}. The maximum force achieved before the ice cube was sheared off the surface was noted and used to calculate the shear strength (*i.e.*, ice adhesion). Since the laser-fabricated surface structures are directional, two sets of measurements were performed to evaluate the ice adhesion strength both perpendicular to the laser-made grooves and parallel to them. In both cases, tests were repeated four times on different areas of each surface.

2.5. Evaluation of corrosion resistance

The corrosion resistance of six types of surfaces developed and used in the study was evaluated on 20 × 20 mm samples. The electrochemical measurements (recording potentiodynamic polarization curves) were performed in a 0.1 M NaCl solution in deionized water. The testing was done in a 250 mL glass cell utilizing a three-electrode configuration. The test sample was fixed to the cell and the tested surfaces served as the working electrode. A saturated Ag/AgCl electrode with a potential of $E = 0.197$ V relative to the standard hydrogen electrode (SHE) was used as a reference electrode, while a 5 mm graphite rod was utilized as a counter electrode. All measurements were performed using a potentiostat/galvanostat Autolab 204 M (Metrohm Autolab) with Nova 2.1

software for data acquisition and results analysis. The potentiodynamic measurements were recorded from −250 mV relative to the open circuit potential with increasing potential in the anodic direction at a rate of 1 mV s^{-1}. The corrosion current density j_{corr} and corrosion potential E_{corr} were determined using the Tafel analysis. Additionally, we determined the potential breakdown E_{bd} and the span between E_{corr} and E_{bd} ($\Delta E = |(E_{bd} - E_{corr})|$).

3. Results and discussion

3.1. Surface morphology, chemistry and wettability

Secondary electron SEM images of the developed functionalized surfaces are shown in Fig. 3, where each column corresponds to one surface. It is evident that the smaller of the two laser scanning line spacing values (25 μm) resulted in a more random surface morphology. While some semblance of channels is evident on surfaces S-25 and D-25, they are highly irregular. The lower spacing also resulted in higher roughness on the micron scale with more redeposited ablation products due to higher energy input density. On the other hand, channels are clearly visible on the two surfaces with the 50 μm spacing between the laser scanning lines. Shallow channels formed on the S-50 surface, while much deeper channels were present on the D-50 surface.

Surface composition was analyzed through an EDS analysis at 5 kV with the analyzed area size ~100 × 100 μm. The results are listed in Table 2. Four expected elements were focused on: oxygen, aluminum, fluorine, and phosphorous. The results show heavy oxidation of all four laser-textured surfaces (the untextured surface exhibits an oxygen content of approx. 3–8 at.% at the same analysis conditions), while fluorine and phosphate detection confirms that FDPA (the fluorinated hydrophobization agent) was successfully grafted onto the surface. On the S-25 surface, a greater amount of phosphorus and fluorine was detected and can be attributed to more efficient grafting of the laser-treated surface with the FDPA molecule. It should be noted that despite performing the EDS at 5 kV, the analysis penetrated deep into the analyzed material (up to a few tens of nanometers). In addition, such a rough and uneven surface affects the accuracy of the results. While it provides a good indication of the general composition of the surface, it cannot fully identify the composition of the topmost (nanometric) surface layer.

Table 2
Results of the EDS analysis of the area in the third line of Fig. 3, performed at 5 kV.

Sample	O (at.%)	F (at.%)	Al (at.%)	P (at.%)
S-25	18.0	32.7	48.0	1.3
S-50	21.5	13.1	64.8	0.6
D-25	24.6	13.5	61.0	0.9
D-50	16.5	9.0	74.0	0.5

Previously performed XPS analysis of a laser-textured 1050A aluminum alloy surface grafted with FDPA has shown that fluorine is the predominant element in the uppermost nanometric surface layer (48.5 at.%), followed by carbon at 25.8 at.% (both a contaminant and a part of the FDPA molecule) and oxygen at 15.9 at.% (also a part of FDPA and found on the heavily oxidized laser-textured surface). Finally, aluminum

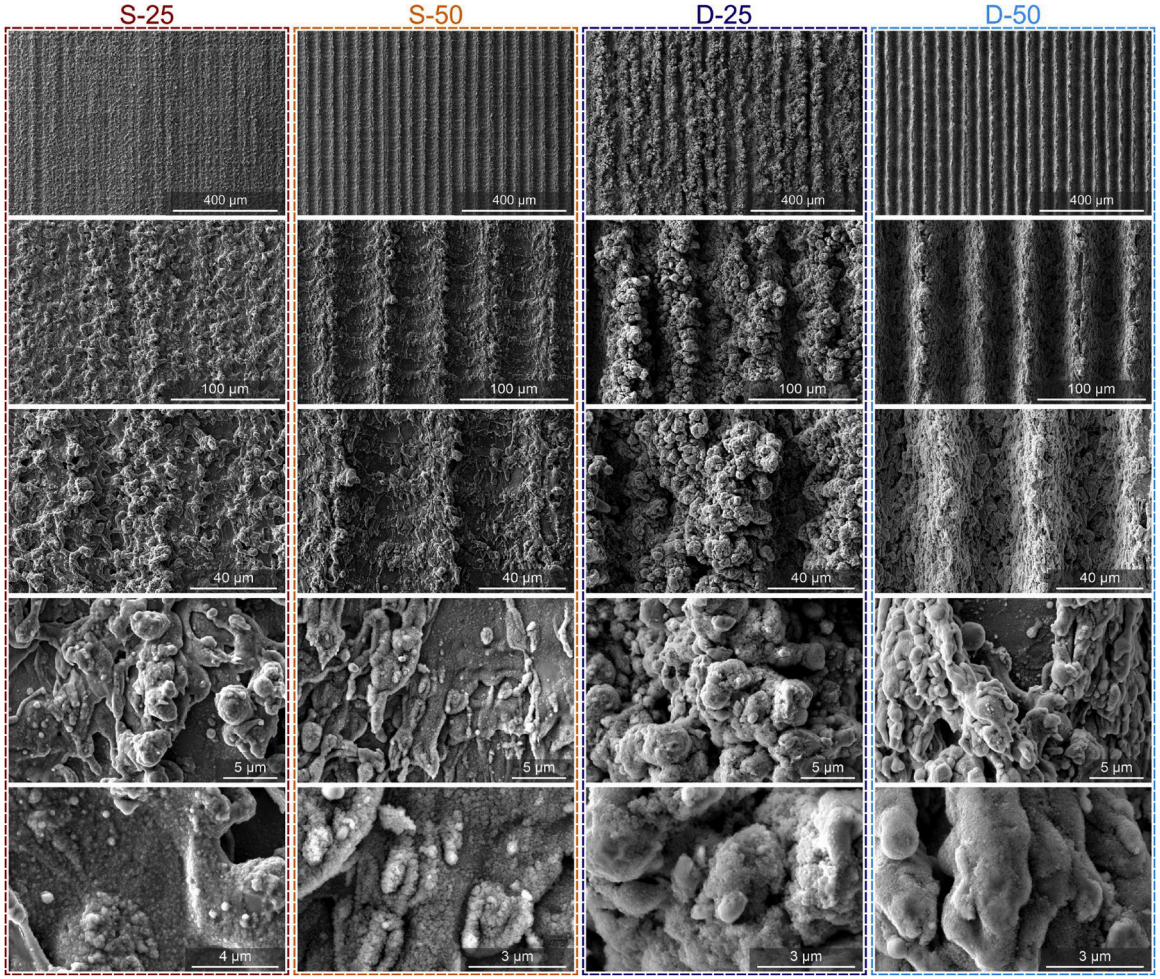

Fig. 3. SEM images of the four laser-textured surfaces developed in this study.

as the predominant material in the 1050A aluminum alloy substrate was detected at 8.4 at.% and phosphorous (present in the FDPA) at 1.5 at.%. This further confirms the successful grafting of the FDPA monolayer onto the laser-textured surface.

The chemical bonding of FDPA molecules to laser-structured aluminum surfaces was further investigated using attenuated total reflectance Fourier transform infrared spectroscopy (ATR-FTIR). Spectra were acquired for bare aluminum and FDPA powder [Fig. 4(a)], and aluminum surfaces laser-structured under different parameters (DT50, DT25, ST50, ST25), both without and with FDPA surface grafting [Fig. 4 (b)].

The FTIR spectra revealed distinct vibrational bands at 1111 cm^{-1}, 1012 cm^{-1}, 663 cm^{-1}, and 643 cm^{-1}, which are attributed to phosphate group vibrations, supporting the presence of P—O—Al surface bonding. Additionally, bands at 1200 cm^{-1} and 1148 cm^{-1}, corresponds to the C—F stretching vibrations in CF_2 and CF_3 groups of the perfluoro tail.

The bonding mechanism of freshly laser-structured aluminum in FDPA/2-propanol solution involves the chemisorption of the phosphonic acid headgroup onto laser-structured (hydroxylated) aluminum surface sites. After exposure to atmospheric moisture, the aluminum surface is hydroxylated [80] and FDPA molecules can undergo condensation with surface hydroxyls.

First-principles calculations have shown that this reaction is exothermic on hydroxylated alumina surfaces with a reaction energy of −114 kJ/mol [81]. Note the reaction energy represents the cumulative effect of bond-breaking and bond-making and the strength of the bond between the phosphonate and the surface is estimated to be around 500 kJ/mol [81], indicating that these molecules will persist on the surface for prolonged periods of time. Compared to weaker physisorption or hydrogen bonding, phosphate-based surface functionalization provides excellent durability, especially under aqueous or corrosive conditions.

The successful anchoring of FDPA via phosphonate binding leads to the orientation of the perfluorinated tails away from the surface [22]. Moreover, with longer alkyl(perfluoro) chains, the surface is effectively covered due to molecular tilting [22], which significantly lowers surface energy and enhances hydrophobicity (corrosion protection).

To quantify the surface topography, profilometric analysis was performed to obtain roughness parameters and compare surface profiles.

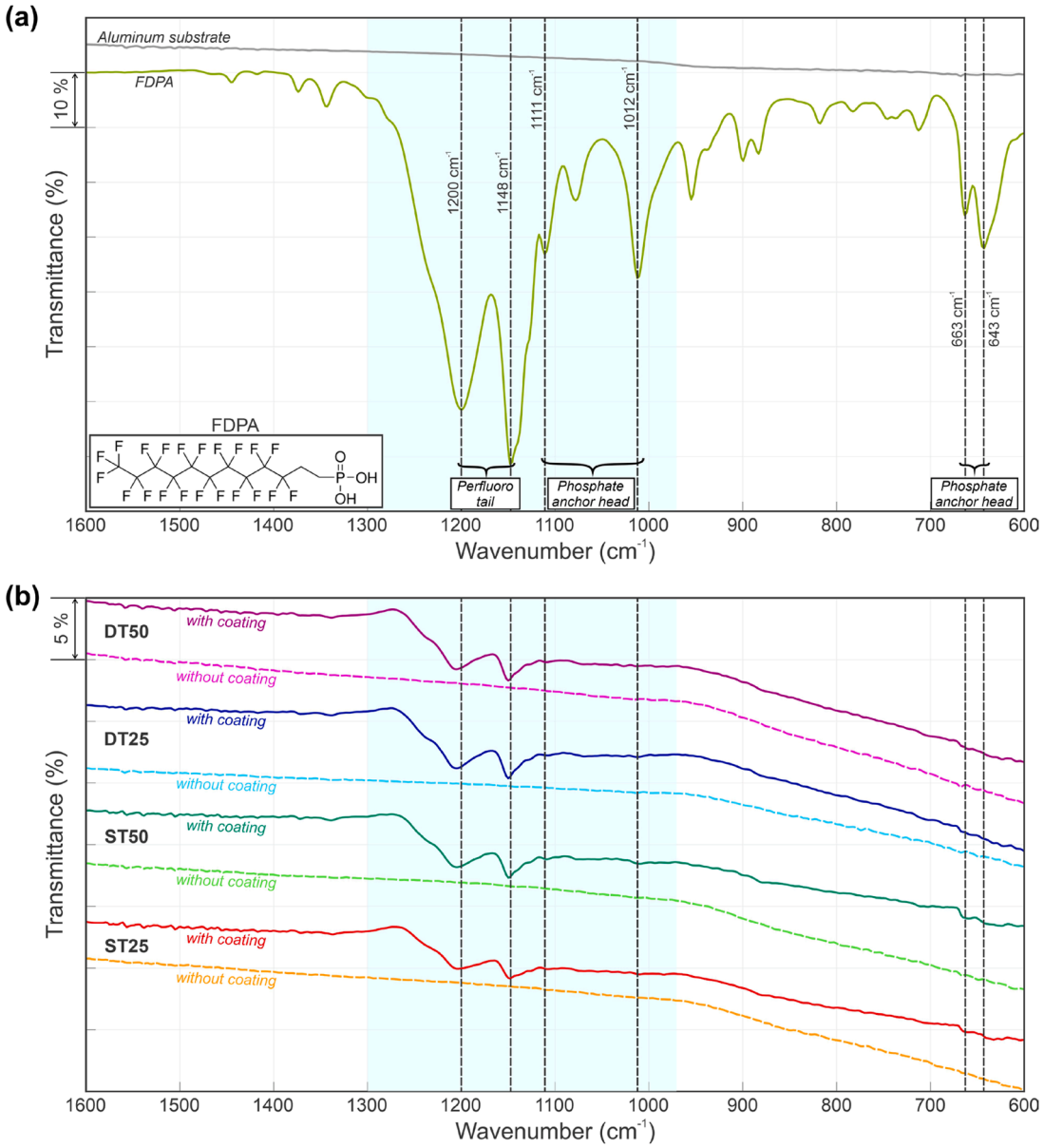

Fig. 4. FTIR analysis of the untreated aluminum substrate and FDPA powder (a) and of the four laser-textured surfaces with and without the grafted FDPA monolayer coating (b).

The results of the analysis are shown in graphical form in Fig. 5, where 3D images of surface profiles are compared, and in Table 3, where the Sa roughness according to ISO 25178 are given alongside with average channel depth and width. The latter values are only given for the two surfaces with 50 μm laser scanning line spacing where the channels are clearly discernible. The results in Fig. 5 are intentionally shown with the same height scale (namely, the range of the color bar) to allow for a direct comparison between the four analyzed surfaces.

The results show that the laser-texturing parameters used to fabricate the shallow surface structures (*i.e.*, the "S" samples) indeed produce far shallower surface structures. Specifically, an average channel depth of 3.1 μm was measured from the surface profiles obtained using a digital microscope, while the average channel width was one order of magnitude greater (23.2 μm) and approximately corresponds to the diameter of the focused laser beam on the surface (~25 μm). The second set of laser texturing parameters, aimed at producing deeper structures with the higher average pulse fluence (*i.e.*, the "D" samples) produced a comparable average width of the laser-made channels (26.8 μm) but significantly deeper structures (26.8 μm), which are one order of magnitude deeper than on the "S" surfaces. This also resulted in notable differences in the roughness values of S_a (arithmetical mean height). While the S-25 and S-50 surfaces exhibited an Sa value of 1.13 μm and 2.39 μm, respectively, the values on the D-25 and D-50 surfaces were much higher at 5.99 μm and 9.18 μm, respectively.

Since the width of the laser-etched channels on the surface (when made with sufficient spacing) was approximately the same as the spacing between the laser scanning lines for the samples with 25 μm spacing (S-25 and D-25), it is clear that irregular surface features formed due to the overlap between the irradiated (and hence ablated) area during subsequent passes of the laser beam across the surface.

Since the interaction of the surface with water is extremely important both for freezing delay/prevention and corrosion protection, water contact angles were evaluated on all surfaces. Dynamic contact angles were measured on the superhydrophobic laser-textured surfaces to evaluate the droplet's spreading and contracting behavior on the surface. The contact angles are provided in Table 4. Dynamic contact angles were not measured on the two reference surfaces; static contact angles were recorded instead. The untreated reference surface (REF)

Table 3
Surface roughness and dimensions of laser-etched microchannels.

Sample	Sa (μm)	Channel width (μm)	Channel depth (μm)	Surface morphology
REF & REF-H	0.6 ± 0.1	/	/	Flat reference surface
S-25	1.1 ± 0.2	/	/	Shallows structures, channels not discernible
S-50	2.4 ± 0.2	23.2	3.1	Periodic shallow channels
D-25	6.0 ± 0.5	/	/	Deep and heavily oxidized structures, highly irregular channels
D-50	9.2 ± 0.6	26.8	26.8	Periodic deep channels

Table 4
Advancing (θ_a) and receding (θ_r) contact angles and the contact angle hysteresis (CAH = θ_a - θ_r) measured on the functionalized surfaces before and after degradation tests.

Sample	Before degradation			After degradation		
	θ_a (°)	θ_r (°)	CAH (°)	θ_a (°)	θ_r (°)	CAH (°)
S-25	167.0 ± 0.9	165.6 ± 1.0	1.4 ± 1.3	166.8 ± 1.4	163.8 ± 1.8	3.0 ± 2.3
S-50	167.2 ± 1.3	163.9 ± 2.5	1.7 ± 2.8	166.6 ± 1.1	164.7 ± 1.5	1.9 ± 1.8
D-25	163.3 ± 0.9	161.8 ± 1.3	1.5 ± 1.5	162.7 ± 0.7	160.8 ± 0.9	1.9 ± 1.1
D-50	165.2 ± 1.1	163.3 ± 1.5	1.9 ± 1.9	164.7 ± 0.7	162.8 ± 1.2	1.9 ± 1.4

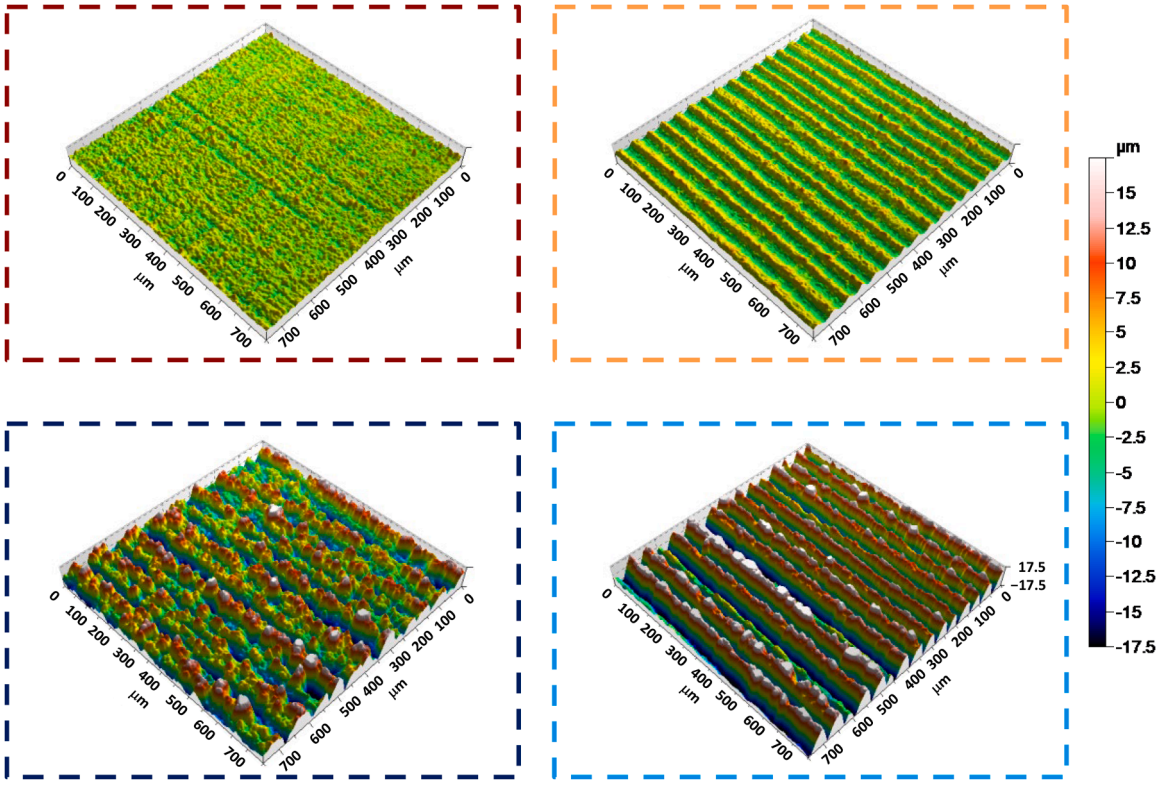

Fig. 5. Profilometric analysis of the four laser-textured surfaces. The range of the color bar denoting the depth of the structure is identical for all four surfaces.

exhibited a static contact angle of 63.4° ± 0.4 °, and its hydrophobized variant (REF-H) exhibited a static contact angle of 117.8° ± 0.4°

The results in Table 4 indicate that the criteria for superhydrophobicity are fulfilled on all four functionalized surfaces with contact angles above 150° and negligible contact angle hysteresis. The roll-off or sliding angles were not measured since the droplet rolled off the surfaces at the slightest inclination. While small differences in contact angles exist between the four prepared surfaces, it is hard to attribute them to the specific surface properties rather than the statistical scatter of the results and uncertainty in the contact angle determination.

Additionally, surface degradation tests were performed to evaluate the stability of the functionalized surface prior to anti-icing experiments since the degradation of the grafted FDPA monolayer could result in a total failure of the surface's icephobic behavior. The following methodology was used to evaluate the degradation of surface wettability and estimate the robustness of the surface. The surface was cooled down to −40 °C and covered with water droplets dripped from a height of ~25 cm (impact velocity ~2.2 m s^{-1}). When the entire surface was covered with ice, it was heated to +40 °C, and the thawed ice was removed. This cycle was repeated 5 times in total and the dynamic contact angles were measured again with the results presented in Table 4 alongside the results before the degradation. Furthermore, the change in the advancing and receding contact angle and the contact angle hysteresis (CAH), calculated as the difference between the values before degradation testing and after it, is plotted in Fig. 6.

Evaluation of the wettability degradation in Table 4 and Fig. 6 shows positive results with minimal changes in the contact angle after the degradation. Specifically, the largest change in contact angle was only 1.8°, indicating favorable robustness of the developed functionalized surfaces and their suitability for the following anti-icing tests.

3.2. Ice nucleation temperature

Ice nucleation temperature was evaluated on all six samples with two different desiccants which provided either 15-20 % relative humidity (silica gel – SG) or <10 % relative humidity (molecular sieves – MS) during the measurements. Relative humidity importantly influences the freezing process as water condensation or direct frosting on the subcooled surfaces can initiate freezing and obscure the observation. Furthermore, humidity significantly influences mass transport between the droplet and the surrounding air. Based on the temperature and relative humidity of the air, droplet evaporation or condensation of water vapor on the droplet can take occur [82]. The ice nucleation temperature measurement results are presented in Fig. 7 as probability density histograms with each subplot showing two sets of experiments (one with each desiccant type) on one surface type. Kernel fit was performed for each distribution (solid lines), and the arithmetic average value for each dataset is shown as a vertical dashed line.

In all cases, the distributions are not symmetrical, with some droplets freezing at significantly higher temperatures than the average ice nucleation temperature on the given surface, resulting in longer left tails for most distributions. On the other hand, few droplets freeze at notably lower temperatures than the average ice nucleation temperature on the given surface, resulting in a short right tail and a skewed distribution. Skewness values are presented in Table 5 and should be interpreted with the reverse direction of the X-axis in the Fig. 7 plots in mind since their sign is thus reversed.

The results are also compared in Fig. 8, where average ice nucleation temperatures are presented for each sample using either silica gel or molecular sieves as the desiccant. We observed a trend of slightly lower or comparable average ice nucleation temperatures at lower relative humidity levels (*i.e.*, with molecular sieves) compared to silica gel. A slight deviation from this trend was observed for the S-50 sample. On the other hand, the difference between the two humidity levels was the most extreme for the D-25 sample with deep structure and irregular channels. For this sample, the distributions shown in Fig. 7(e) are very narrow (especially for the molecular sieves) and the average nucleation temperatures are higher (*i.e.*, showing a worse performance) than on the untreated or the solely hydrophobized sample. This sample partially exhibited cascade freezing behavior with most or all drops freezing at the same time (and temperature) during the tests. This will be shown and discussed further in Section 3.4.

Ambient humidity can play a significant role in determining the ice nucleation temperature of sessile droplets, particularly through its influence on surface structure, interfacial wetting, and heat transfer dynamics. Since superhydrophobic surfaces are typically rough and feature low surface energy, both of which are required to maintain a heterogeneous (*i.e.*, Cassie–Baxter) wetting state where the droplet rests

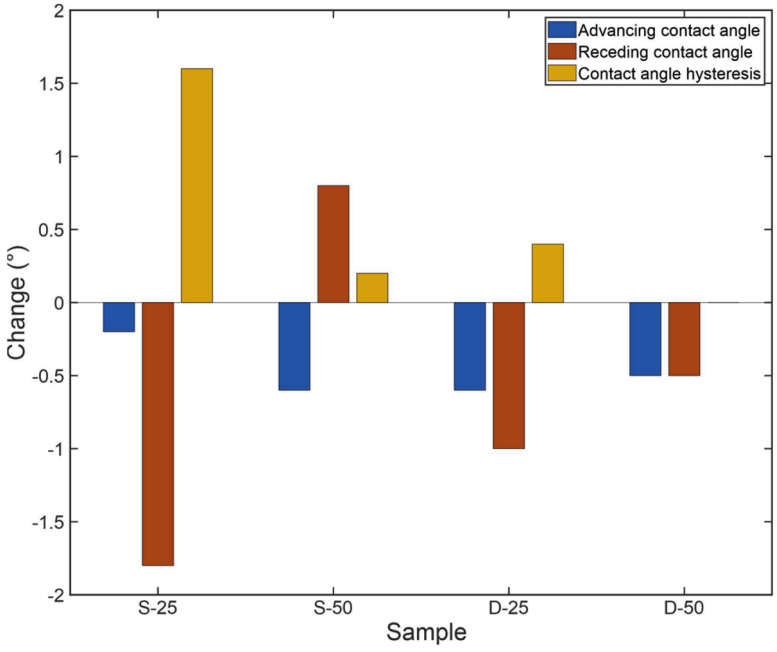

Fig. 6. Change of the dynamic contact angle values and the contact angle hysteresis after degradation testing with cyclical icing/deicing.

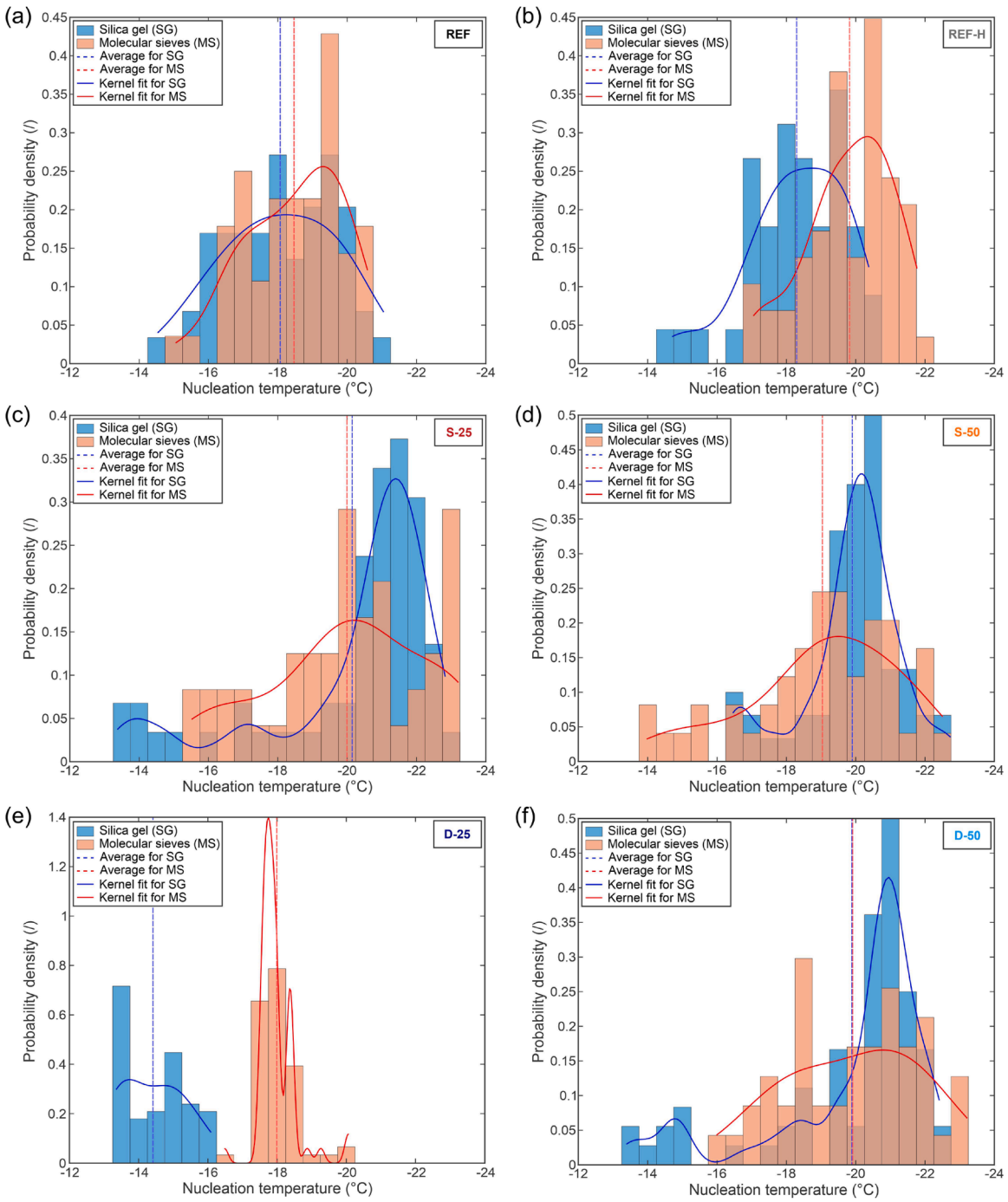

Fig. 7. Distribution of ice nucleation temperature on (a) untreated reference sample, (b) hydrophobized reference sample, (c) S-25 sample, (d) S-50 sample, (e) D-25 sample, and (f) D-50 sample. Silica gel (SG) and molecular sieves (MS) provide relative humidity values of 15–20 % and <10 %, respectively.

Table 5
Skewness of the ice nucleation temperature distributions shown in Fig. 7.

Surface	REF	REF-H	S25	S50	D25	D50
Higher rel. humidity (silica gel – SG)	0.109	0.499	1.385	0.701	−0.169	1.518
Lower rel. humidity (molecular sieves – MS)	0.353	0.413	0.238	0.443	−1.602	0.116

partially on trapped air pockets. The preservation of this state is critical to maintaining delayed ice nucleation and icephobic behavior. At a high relative humidity, water vapor can adsorb or condense within the micro- and nanoscale surface textures, which is actually facilitated by the low surface energy of the surface. This capillary condensation can compromise the Cassie–Baxter state by locally filling the surface features, resulting in a (local) transition to the Wenzel homogeneous wetting state. This transition increases the solid–liquid contact area, which enhances heat and mass transfer. Importantly, condensation in the micro-/nanostructures provides "pre-activated" nucleation sites where ice can form with a lower nucleation energy barrier, thus leading to higher nucleation temperatures (*i.e.*, lower required supercooling).

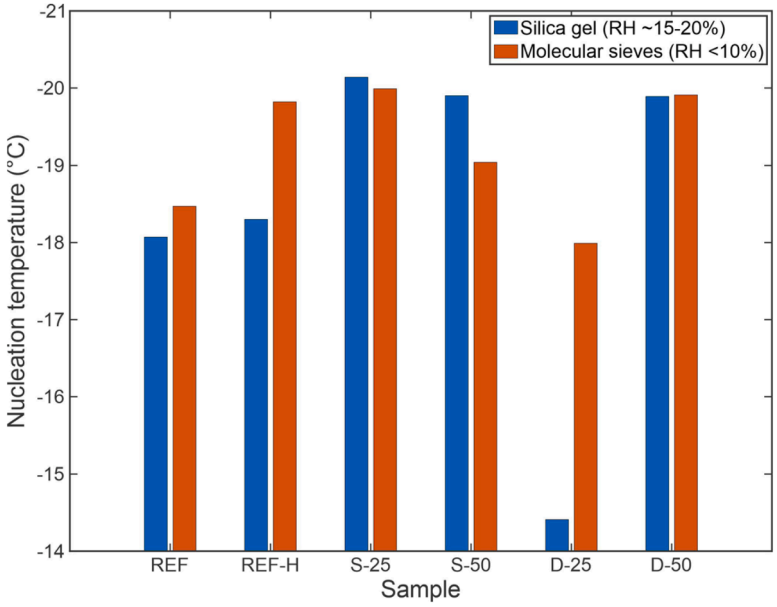

Fig. 8. Average ice nucleation temperatures recorded using silica gel or molecular sieves as the desiccant.

At low ambient humidity, evaporation of the droplet is more pronounced, leading to notable evaporative cooling, which can significantly lower the droplet temperature and allow it to reach higher supercooling values before nucleation. This additional cooling expedites the entire process of droplet cooling and thus reduces the time during which water is in contact with potentially active nucleation sites on the surface. Since nucleation is a stochastic process, the longer the time of contact, the higher the probability of nucleation. Therefore, slightly faster cooling of the droplet can delay heterogeneous nucleation.

All of the above appears to be especially strongly expressed on the DT25 surface, which, judging from the SEM images in Fig. 3, provides an abundance of potential active nucleation sites for condensation of water vapor and nucleation of ice. Here, the largest difference in the nucleation temperature was observed when the humidity was decreased, confirming the critical role of condensation of water vapor (even if present in small amounts) into the surface micro-/nanostructures, which can lead to "premature" ice nucleation.

3.3. *Freezing delay*

A typical metric for quantifying the anti-icing performance of functionalized surfaces is the temporal freezing delay. Hence, the time needed for a droplet to freeze on a surface at a given (subzero) temperature is measured on each of the analyzed surfaces. We performed the measurement at three selected temperatures (−15 °C, −17.5 °C, and −20 °C) with multiple repetitions with multiple droplets for each surface, and the obtained average values are shown in Fig. 9. Firstly, the typical trend of decreasing freezing delay with decreasing surface temperature was observed, with delays of upwards of 2500 s at -15 °C falling to below 800 s at -20 °C [83,84]. The two surfaces with shallow channels (S-25 and S-50) exhibited the best performance in the form of the longest average freezing delays. At −15 °C, the S-25 and S-50 surfaces granted

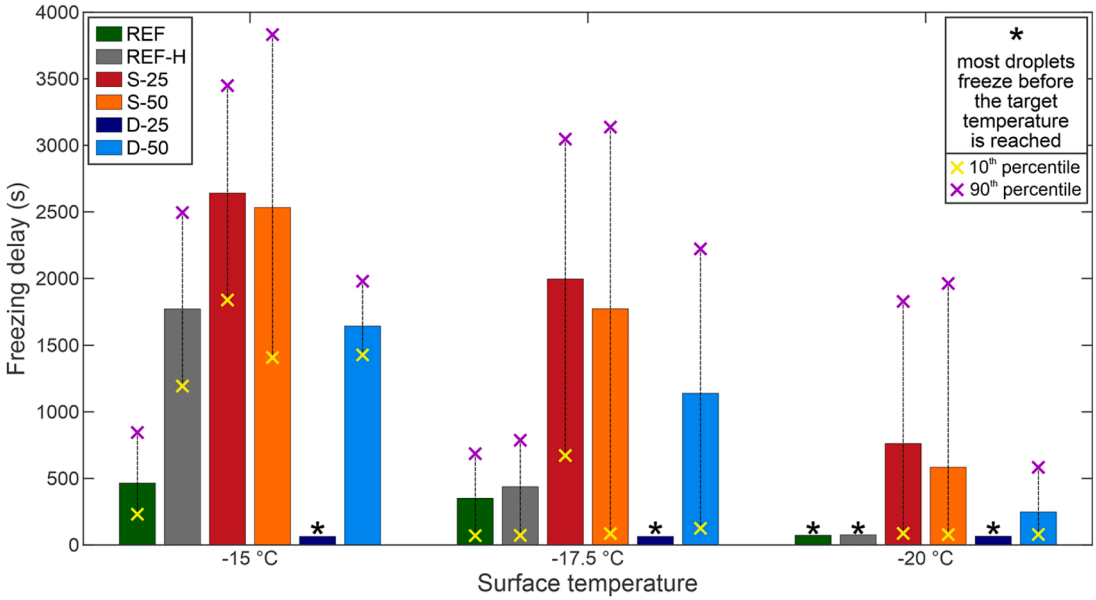

Fig. 9. Average freezing delay recorded on all six tested surfaces at three surface temperatures. 10th and 90th percentile limits of the scatter of the measured freezing delays are shown with yellow and pink crosses, respectively.

an average freezing delay of 2641 s and 2533 s, respectively, compared to 465 s on the untreated surface. The surface with well-spaced deep channels (D-50) also exhibited favorable, albeit lower performance. On the other hand, the surface with irregular deep channels (D-25) exhibited the worst performance, even underperforming the untreated reference surface. This can be attributed to higher ice nucleation temperatures, which resulted in most of the droplets freezing even before the surface reached the target temperature of the individual test. While the hydrophobized untreated surfaces (REF-H) exhibited marginally lower ice nucleation temperatures as shown in Figs. 7–8, its freezing delay was notably longer compared to the completely untreated surface (REF) at −15 °C. However, at lower surface temperatures comparable to or lower than the respective nucleation temperatures of the aforementioned surfaces, the performance of the REF-H surface was largely the same as that of the REF surface.

Additionally, the freezing delay enhancement is shown in relative terms in Fig. 10 for the hydrophobized reference surface and the three functionalized surfaces that exhibited favorable behavior (S-25, S-50, and D-50). The best performance was observed on the S-25 surface with hardly discernible laser-etched channels and the lowest surface roughness among the laser-textured surfaces. On this sample, the lowest (and thus the most favorable) ice nucleation temperatures were also observed. The S-25 surface exhibited an increase in freezing delay of 468 % at -15 °C and 944 % at -20 °C. The superior performance of the shallow surfaces in comparison with the deep surfaces may be attributed to a lower number of cavities and other morphological features that could serve as active nucleation sites for condensation and freezing of water. SEM images in Fig. 3 reveal that the deep surface textures, fabricated using a higher laser pulse fluence, contain many cavities and crevices on the micron and submicron level, which matches the most suitable size range for nucleation of water vapor [85]. This is most extremely evident on the D-25 surface (see SEM images in Fig. 3), where the concentration of the energy input was the highest due to the combination of high pulse fluence and low laser scanning line spacing. On the other hand, such unwanted features are largely absent from the two surfaces with shallow structures, where some splashing of the material during the laser-texturing occurred, but few cavities or similar structures formed.

3.4. Observation of the freezing process

We also visualized the freezing process and tracked the progression of the freezing (solidification) front on three representative surfaces, namely on the untreated reference surface, the hydrophobized reference surface, and a superhydrophobic laser-textured surface (S-50). The vertical position of the solidification front is given in normalized terms using the final height of the droplet (*i.e.*, when completely frozen) for normalization; the results are shown in Fig. 11. The freezing process from the onset of the solidification to the completion of freezing was by far the fastest on the untreated surface, which exhibited the highest wettability and thus the highest contact area with the subcooled surface (approx. 10.2 mm^2). Since the Wenzel wetting regime was present, there was no air between the surface and the droplet to limit the heat transfer from the droplet to the surface. The hydrophobized reference surface with no laser-textured features exhibited 348 % longer solidification time compared to the more wettable completely untreated surface with no hydrophobic coating, which should be attributable to the reduced contact area between the surface and the droplet (~4.0 mm^2) due to the significantly higher contact angle (~117°). Finally, the superhydrophobic surface, which exhibited the Cassie-Baxter wetting regime with only limited contact between the solid surface and the droplet, granted even longer solidification times (1185 % longer than the untreated reference surface and 186 % longer than the hydrophobized reference surface). Here, the heat transfer is limited due to two factors: *(i)* the even smaller (projected) contact area between the surface and the droplet (~0.30 mm^2) and *(ii)* the actual solid-liquid (and later solid-solid) contact area being significantly smaller than the projected contact area since the droplet is locally suspended on the peaks of micro-/nanostructure with an air layer partially separating the droplet and the surface.

The observed cascade freezing phenomenon on the D-25 surface was analyzed further with a dedicated experiment, the results of which are shown in Fig. 12(a,b). To investigate the very narrow distributions of the ice nucleation temperature and the very poor anti-icing performance of this surface with deep irregular channels, a set of 7 μL droplets was deposited on the surface and an ice nucleation temperature measurement was conducted, this time without focusing on the temperature but rather on observing the set of droplets with a higher framerate and higher magnification. The results of the first measurement are shown in Fig. 12(a). The first droplet froze approx. 10 s before the cascading event

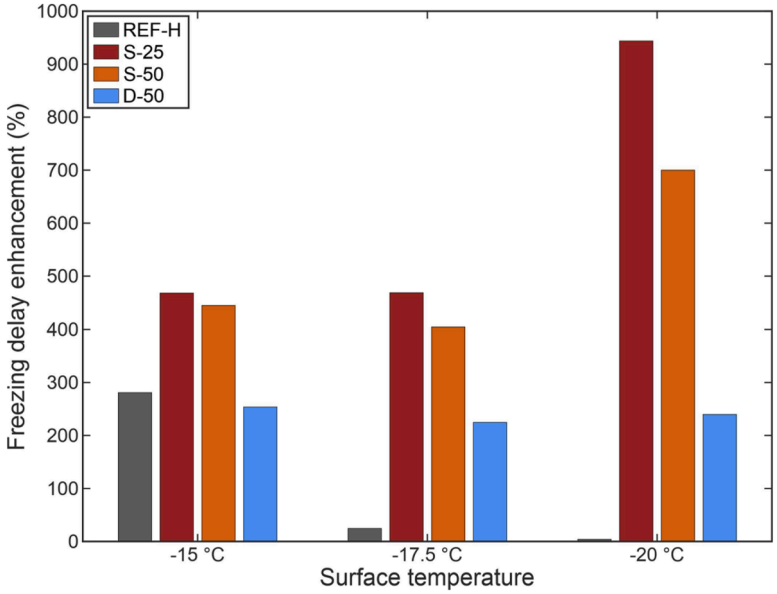

Fig. 10. Relative enhancement (*i.e.*, prolongation) of the freezing delay achieved with functionalized surfaces compared to the untreated surface.

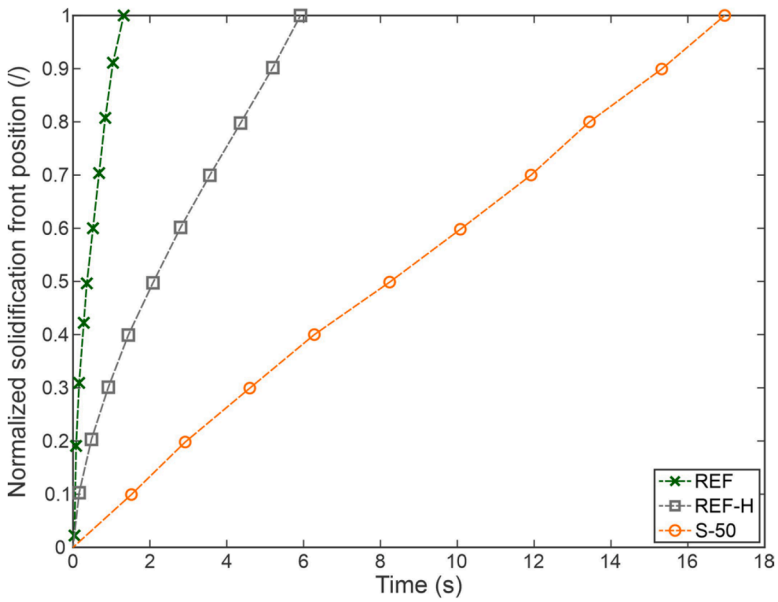

Fig. 11. Normalized vertical position of the freezing front during droplet solidification on three representative surfaces.

happened. The cascade included almost simultaneous nucleation of 7 droplets, spaced between approx. 1.5 and 8 mm from one another, with the recalescence in all of them appearing within 160 ms. Interestingly, several remaining droplets failed to freeze in the cascade despite being a similar distance away from the cascading droplets. Two examples of remaining droplets freezing with a delay of approx. 13 s and 17 s from the onset of the cascade are shown in Fig. 12(a).

The second experiment focused on another set of droplets, which were imaged using higher spatial and temporal resolution. The results show that all seven droplets present started freezing within 60 ms of the recalescence of the first droplet. The experiment was repeated multiple times and on two separate surfaces with the same observation being made every time. No frost halos or ice bridges were observed, and the droplets didn't explode or shatter to release ice particles.

Jung et al. [86] reported the formation of frost halos around freezing droplets due to their evaporation which were shown to possibly initiate the freezing of neighboring droplets. However, both the observed timescale (~0.1 s) and length scale (<0.5 mm) of this phenomenon do not match our observations since the cascade freezing of neighboring droplets happened both faster (<0.02 s) and over a greater distance (between approx. 1 and 5 mm). Graeber et al. [87] were the first to report and systematically investigate the phenomenon of cascade freezing among supercooled droplets, although previous reports of freezing propagation via the aforementioned frost halos [86], ice bridging [88] or ice shrapnel exist [89]. They proposed that cascade freezing is caused by airborne vapor boluses (emitted by the freezing droplet), generated and rapidly propagated into the surroundings during the recalescence of supercooled droplets. When the vapor bolus reaches a supercooled neighboring droplet, it can cause local supersaturation and spontaneous formation of microscopic ice crystals by heterogeneous nucleation condensation on airborne dust and subsequent solidification, triggering nucleation by contact freezing of the neighboring droplet. However, their measurements were performed in a low-pressure environment where the vapor diffusion speed was much greater than at atmospheric pressure (approx. 1 m s^{-1} and 0.003 m s^{-1}, respectively). Therefore, this seems unlikely to be the reason behind the cascade freezing observed in the present study.

Fletcher [90] reported the reduction of the free energy barrier in the case of heterogeneous nucleation ΔG_{het} instead of homogeneous nucleation ΔG_{hom}, described by a factor f with a value between 0 and 1:

$$\Delta G_{het} = \Delta G_{hom} f \tag{1}$$

According to Jung et al. [91] and Fletcher [90], the parameter f depends primarily on the size and wettability of the surface upon which the nucleation is taking place. Since the majority of the surface features on all surfaces used in this study are orders of magnitude larger than the critical radius for nucleation (the latter being on the approximate size scale of nanometers), f should primarily depend on the contact angle θ [91]:

$$f \approx f(\theta) = \frac{\left(2 + \frac{\gamma_I - \gamma_W}{\gamma_{IW}}\cos\theta\right)\left(1 - \frac{\gamma_I - \gamma_W}{\gamma_{IW}}\cos\theta\right)^2}{4} \tag{2}$$

where γ_I, γ_W and γ_{IW} represent the ice–gas, water–gas, and water–ice interfacial tensions, respectively. However, the contact angle on all four laser-textured surfaces is practically identical, excluding its effect on the reduction of nucleation energy barrier as described by the factor f.

Going further, the cascade freezing phenomenon together with significantly higher nucleation temperatures on the D-25 surfaces compared to the other three superhydrophobic laser-textured surfaces likely should be attributed to the specific micro- and nanostructure of the D-25 surface. Furthermore, lower ambient humidity significantly decreased the nucleation temperatures on the D-25 surface (Fig. 7), but the cascade freezing phenomenon persisted as evident from the narrow nucleation temperature distributions in Fig. 7(e). High-magnification SEM images of the D-25 surface showing structures ranging from several micrometers and down to tens of nanometers are shown in Fig. 12(c). We postulate that the micro- and nanostructure of the D-25 surface provided preferential nucleation sites for condensation of water vapor from the air within the experimental chamber. This is further substantiated by the difference in nucleation temperatures for the two sets of measurements at different humidity levels. At higher humidity (using silica gel as the desiccant and achieving a relative humidity of 15–20 %), the average nucleation temperature was 3.6 K higher than during the experiments with lower humidity (using molecular sieves as the desiccant and achieving a relative humidity below 10 %). It can be assumed that higher humidity resulted in more condensation on the surface at the same surface temperature as saturation was more readily reached at the given air temperature, resulting in frosting and possible spreading of ice at the foot of the droplets on the D-25 surface, consequently contributing to the "premature" freezing of the droplets.

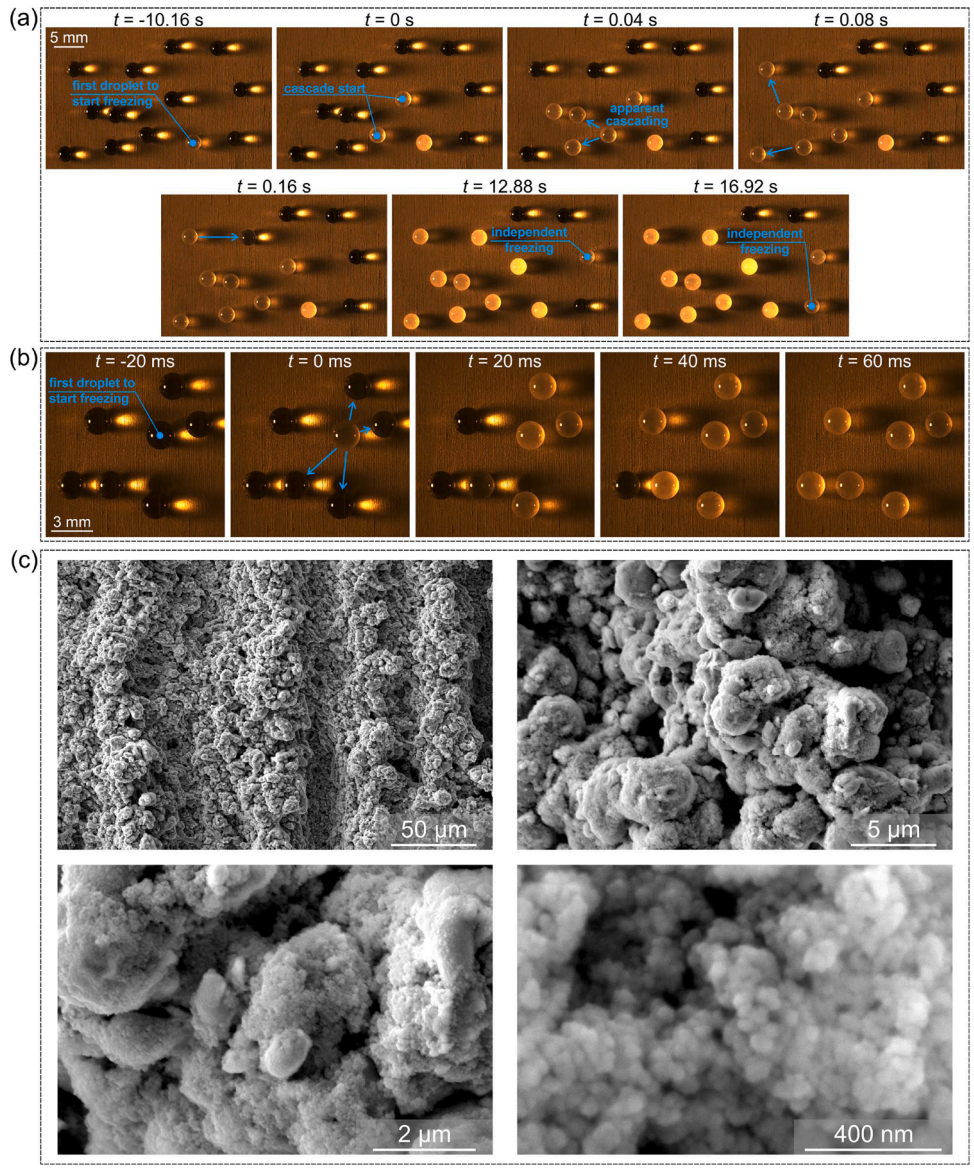

Fig. 12. The process of cascade freezing on the surface D-25 (a), localized analysis of cascade freezing (b) and (c) secondary electron high-magnification SEM images of the D-25 surface's morphology showing cavities and cavity-like structures on various length scales.

3.5. Ice adhesion strength

The results of ice adhesion measurements are shown in graphical form in Fig. 13(a) as absolute average values with standard deviation shown through error bars, while a relative comparison to the untreated reference surface is shown in Fig. 13(b).

Together with the hydrophobized reference surface (REF-H), both functionalized surfaces with shallow structures (*i.e.*, S-25 and S-50) provided reduced ice adhesion strength. Specifically, the REF-H surface decreased the adhesion by approx. 51 %, the S-25 surface by 21–26 % and the S-50 surface by 45–60 %. On the S-25 surface, which features a non-distinct surface morphology and low surface roughness, minimal difference between adhesion strength parallel or perpendicular to the laser-made grooves was observed. On the other hand, a more notable difference was measured on the S-50 surfaces with shallow channels where a 27 % lower average adhesion value was obtained in the perpendicular testing direction compared to the parallel testing direction.

On the other hand, notably higher ice adhesion strength was measured on the surfaces with deep features (*i.e.*, D-25 and D-50) with an increase of up to 84 % in comparison with the untreated surface. On the D-25 surface with highly irregular channels, the adhesion was 15 % higher when evaluated parallel to the direction of the channels compared to the values measured perpendicular to the channel direction. On the other hand, the opposite trend was observed on the D-50 surface with periodic deep channels with a 25 % lower average value observed in the perpendicular direction compared to the parallel testing orientation.

3.6. Corrosion protective behavior

The corrosion properties for REF, REF-H and the functionalized surfaces (S-25, S-50, D-25 and D-50) were evaluated using potentiodynamic measurements in a 0.1 M NaCl solution after one hour of immersion, as shown in Fig. 14(a,b). Additionally, Fig. 14(c) schematically presents the bonding of the FDPA onto a treated surface and the mechanism of corrosion protection with trapped air between the surface and the corrosion medium. The determined electrochemical parameters are also summarized in Table 6.

Fig. 14(a) illustrates that the curve for reference aluminum (REF)

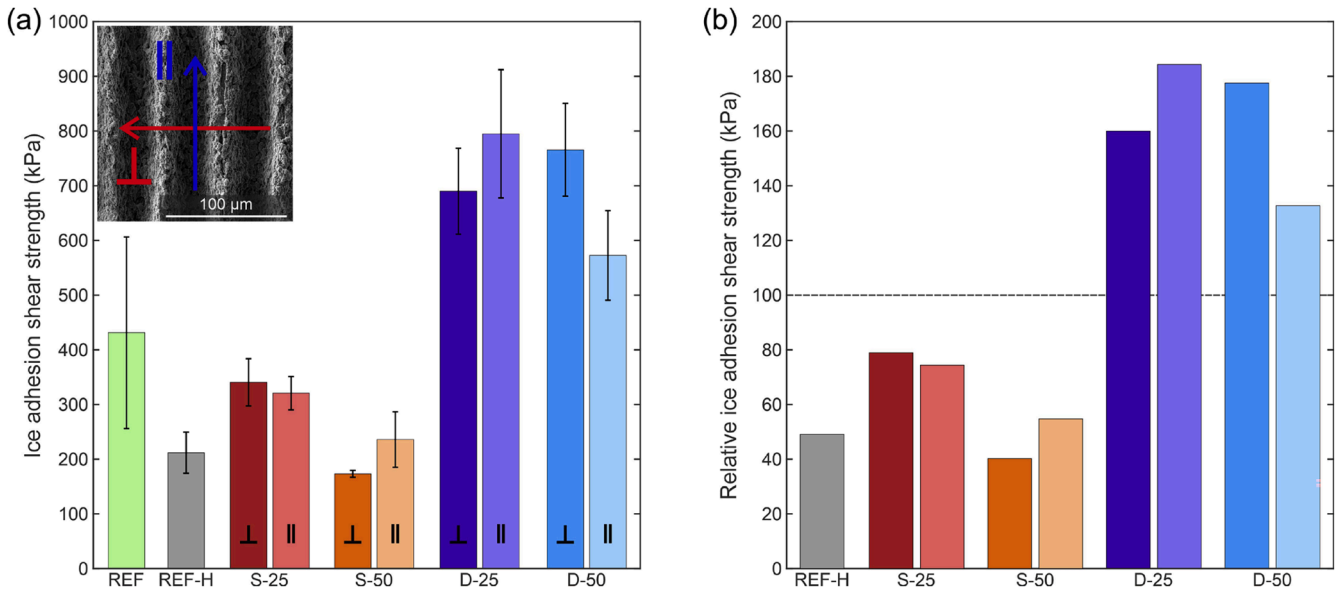

Fig. 13. Ice adhesion strength shown in absolute terms (a) and relative to the average value for the reference surface (b). The inset in subplot (a) shows the testing direction, which is either parallel to the orientation of laser-made structures (∥) or perpendicular to them (⊥).

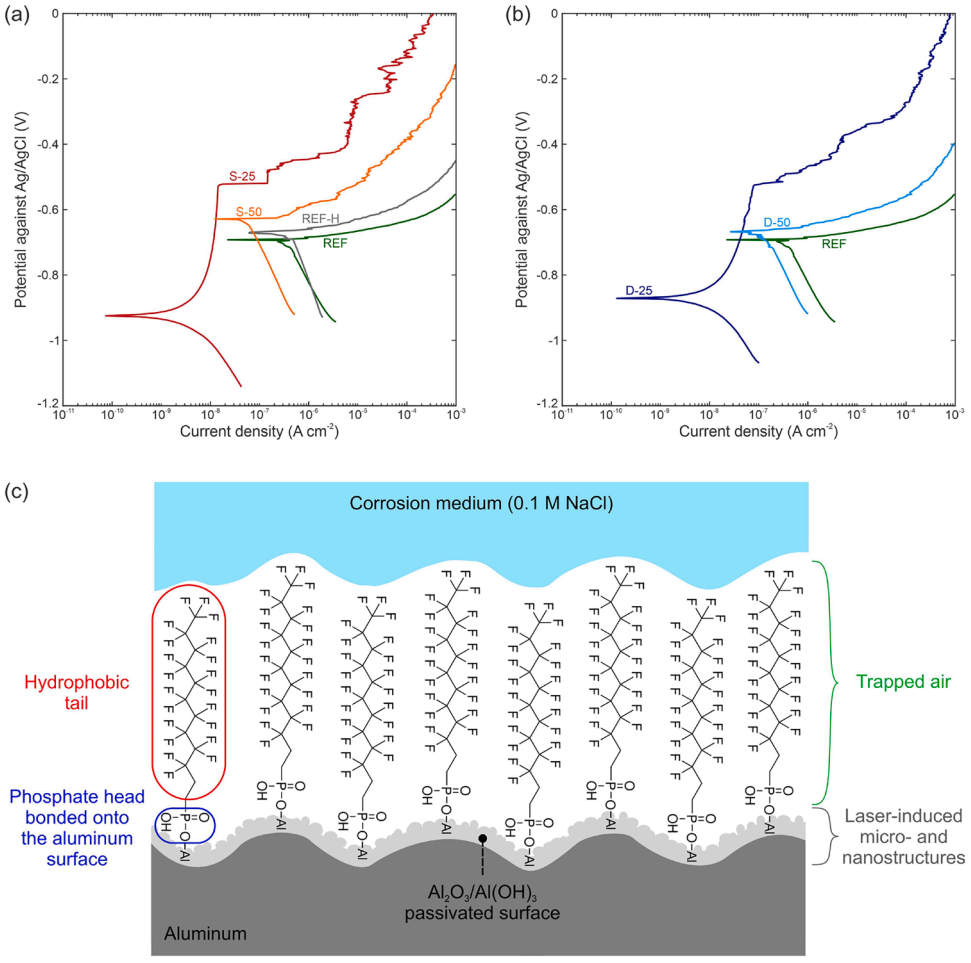

Fig. 14. Potentiodynamic polarization curves for the surfaces with shallow structures (a) and deep structures (b), and (c) schematic representation of the FDPA bonding onto the surface and corrosion protection mechanism with an entrapped layer of air.

Table 6
Evaluated electrochemical parameters with standard deviation in 0.1 M NaCl for REF and REF-H and treated aluminum with S-25, S-50, D-25 and D-50: corrosion current density (j_{corr}), corrosion potential (E_{corr}) and potential breakdown (E_{bd}) were determined from potentiodynamic polarization curves in Fig 14(a,b). The span is expressed as ($\Delta E = |E_{bd} - E_{corr}|$).

Sample name	j_{corr} (nA cm^{-2})	E_{corr} (V)	E_{bd} (V)	ΔE (mV)
REF	426.1	−0.69	−0.68	10
REF-H	415.3	−0.67	−0.66	10
S-25	2.0	−0.92	−0.52	400
S-50	62.3	−0.63	−0.62	10
D-25	8.1	−0.87	−0.53	340
D-50	152.6	−0.67	−0.66	10

exhibits a low corrosion current density (j_{corr} = 426.1 nA/cm^2) and a corrosion potential (E_{corr}) of −0.69 V. Despite the natural passivation of aluminum surfaces with thin Al_2O_3 film under atmospheric conditions reflect efficient corrosion protection, the passivation effect is significantly reduced under the tested conditions during immersion in NaCl solution [21,92,93]. Chloride ions can penetrate and disrupt the thin oxide layer, causing localized breakdown, leading to local corrosion. This breakdown occurs due to the aggressive nature of Cl^- ions that can replace oxygen atoms in the passive layer, forming soluble aluminum chloride complexes and exposing the underlying metal to attack further. This behavior was confirmed by potentiodynamic measurement, where the potential breakdown (E_{bd}) was <10 mV less negative than E_{corr}, resulting in a very narrow passivation region (ΔE), as evident in Fig. 14 (a) and Table 6.

Similar corrosion behavior was also noticed for REF-H (hydrophobized surface), shown in Fig. 14(a). Due to the naturally passivated surface with stable Al_2O_3, the FDPA was not efficiently covalently bonded on the surface to form a protective barrier, and as a result, the formed film could not protect the surface completely. Therefore, there is only a slight decrease in j_{corr} (415.3 nA/cm^2) when E_{corr} shifts to less negative values (−0.67 V), Table 6. Despite the hydrophobic behavior of the surface, the electrochemical results confirmed a limited effect on corrosion protection.

On the other hand, gradually better corrosion protective performance was obtained on the laser-treated surfaces with shallow structures (*i.e.*, S-25 and S-50). The j_{corr} for S-25 is shifted for >2 orders of magnitude to lower values j_{corr} to 2.0 nA/cm^2, E_{corr} to −0.92 V and E_{bd} at −0.52 V, Table 6. It can be assumed that laser treatment removes the native oxide layer on the aluminum surface (Fig. 3) and forms a newly passive film through oxidation [7]. Such passive film composition formed in an oxygen-containing atmosphere (*i.e.*, air) in the presence of laser energy (ablation) differs from the composition of naturally formed film in the atmosphere [94]. From the electrochemical point of view, this effect is reflected in the shifts of E_{corr} to more negative values for >230 mV for S-25 compared to REF, which reflects freshly formed $Al_2O_3/Al(OH)_3$ surface. The laser texturing process creates micro- and nano-scale patterns on the aluminum surface (see Fig. 3). These textures increase the surface area and create roughness, which is essential for enhancing the surface's hydrophobicity when combined with chemical treatments such as FDPA. FDPA molecules contain a phosphonic acid group (–PO(OH)₂) [95,96], which can chemically bond with the aluminum oxide layer on the surface which is schematically depicted in Fig. 14(c). The phosphonic acid group is highly effective in the corrosion inhibition of aluminum due to its strong affinity for metal oxides and its ability to form stable, protective layers on the metal surface, anchoring the FDPA molecules firmly to the surface [96]. The reaction can be represented as:

$$Al - OH + R - PO(OH)_2 \rightarrow Al - O - PO(OH)R + H_2O \quad (3)$$

where R represents the long-fluorinated tails. This reaction results in the formation of an Al—O—P linkage. Once the FDPA molecules are chemically bonded to the surface, they arrange themselves into a monolayer due to van der Waals interactions between the long-fluorinated tails [22]. This self-assembled monolayer (SAM) creates a densely packed, highly ordered structure on the aluminum surface as shown in Fig. 14(c). The fluorinated tails of the FDPA molecules protrude outward from the aluminum surface, creating a highly hydrophobic surface. The low surface energy of the fluorinated tails causes water droplets to bead up, due to the trapped air between the surface and corrosion medium.

Efficient functionalization of the freshly laser textured $Al/Al_2O_3/Al(OH)_3$ surface and FDPA molecule surface reduces the corrosion current density and the efficient superhydrophobic surface's formation is reflected in the passivity region between the corrosion potential E_{corr} and the potential breakdown E_{bd}. In this region, the current density only slowly increases with increasing potential, confirmed by the results in Fig. 14(a). The span between potentials ΔE $|(E_{bd}-E_{corr})|$ was 400 mV, which confirmed a stable passivation region in wide potential ranges. Such behavior is noticeable on a well-protected aluminum surface. Less improved corrosion resistance was noticed for S-50 surface, where the j_{corr} was less than one order of magnitude lower (62.3 nA/cm^2) than on the REF surface with a slight shift of E_{corr} to less negative values, but with E_{bd} is only a few mV above (ΔE = 10 mV). Such behavior can be explained by a less efficient lasering structuring of the surface, as seen in Fig. 3. Due to the remaining weak areas of the non-structured surface, the corrosion protection is less efficient. Despite the surface treatment allowing the formation of a superhydrophobic surface, its corrosion resistance is limited, probably due to an uneven FDPA film on the surface. Therefore, the corrosion media (ions) can contact the aluminum surface, causing less efficient corrosion protection.

A similar comparison was made for the two surfaces with deep structures (*i.e.*, D-25 and D-50) in Fig. 14(b). The laser-textured surfaces with non-distinct surface features produced using the smaller (25 μm) spacing (D-25) show at least two orders of magnitude lower corrosion current density in comparison with the untreated surface (REF). The E_{corr} is again and has shifted to more negative values (−0.87 V). The curve shows the passive behavior with E_{bd} = −0.53 V, while ΔE is 340 mV. On the other hand, the surface with distinct microchannels (D-50) provides less favorable corrosion protection with only a slight decrease in the corrosion current density (152.6 nA/cm^2). On the D-25 surface, a notably higher E_{bd} also appears compared to the REF surface, confirming corrosion resistance of the surface in the anodic part, achieved through passivation.

Overall, hydrophobization of the reference sample with the FDPA self-assembled monolayer failed to contribute significantly to its corrosion resistance since the REF-H sample exhibits the same E_{corr} and j_{corr} values compared to the REF sample. Both laser-textured surfaces with close scanning line spacing significantly improve corrosion protection, with the S-25 surface exhibiting slightly better corrosive protective properties than the D-25 surface. In combination with the low-surface-energy FDPA monolayer and entrapped air in the surface microstructure (due to its superhydrophobic wetting properties), this prevents access of corrosive ions in the water (specifically Cl^-ions due to testing in a NaCl solution) to the surface and the aluminum passivated under atmospheric conditions [4–6].

Laser texturing poses challenges in precision and repeatability due to material-dependent factors such as composition, surface roughness, and oxidation state, which affect the absorption of laser light and the melting/ablation process. Optimization is required for each material to achieve the desired surface properties. Scaling up laser texturing for bulk processing is feasible by adjusting key parameters to favor formation of irregular surface features through strategies such as defocused beam processing, higher scanning speeds, and multi-pass texturing that enable the generation of effective anti-corrosive surfaces. While complex sample/surface geometries introduce additional challenges, advanced positioning systems and hybrid processing approaches (such as sample pre-treatment through mechanical or chemical methods) can

help mitigate these issues, and overall, laser texturing remains a scalable and viable method for achieving anti-corrosive and superhydrophobic properties on bulk samples with proper laser-texturing parameter control.

4. Conclusions

This study presents the fabrication and evaluation of functionalized superhydrophobic aluminum alloy surfaces, produced with a combination of laser texturing and self-assembled monolayer grafting, with enhanced anti-icing and corrosion protection properties. The following main findings were made.

1) The developed surfaces exhibited superhydrophobicity with contact angles $> 163°$ and a hysteresis $< 2°$ Wettability remained stable after five icing/deicing cycles between -40 °C and $+40$ °C.
2) Three out of four surfaces lowered the ice nucleation temperature, with the S-25 surface (shallow, non-distinct features) exhibiting the lowest average value at -20.1 °C. Lower humidity further reduced nucleation temperatures.
3) Functionalized surfaces significantly extended freezing delay with enhancements up to 468 % and 944 % compared to an untreated surface at -15 °C and -20 °C, respectively.
4) Shallow-structured surfaces showed better anti-icing performance than deep-structured ones, ascribed to fewer potential active nucleation sites ice nucleation and for condensation.
5) Repeated cascade freezing was observed on a surface with irregular deep structures, abundant microscale cavity-like structures, and heavy laser-induced oxidation. Relative humidity affected the ice nucleation temperatures, alluding to the effect of preferential condensation and subsequent freezing of water vapor in the available surface features.
6) Surfaces with shallow features decreased ice adhesion strength by up to 60 %, while increased adhesion (between $+33$ and $+84$ %) was measured on surfaces with deep features.
7) Surfaces with non-distinct or irregular channels exhibited better corrosion properties than surfaces featuring well-defined laser-etched channels, with corrosion current density below 10^{-8} A cm^{-2} and a broad passivation region.

The surface with a non-distinct morphology and the lowest surface roughness out of all developed surfaces exhibited the best properties in all evaluations. These results support focusing future designs on micron- and submicron-scale features over traditional larger structures. The demonstrated functionalization approach is promising for scalable industrial applications, offering combined benefits in durability, anti-icing, and corrosion protection.

Data availibility

The authors confirm that the data supporting the findings of this study are available either within the article and from the corresponding author upon request.

CRediT authorship contribution statement

Matic Može: Writing – original draft, Visualization, Software, Methodology, Formal analysis, Data curation, Conceptualization. **Peter Rodič:** Writing – review & editing, Methodology, Investigation. **Tim Štrus:** Writing – review & editing, Methodology, Investigation, Data curation, Conceptualization. **Miha Štucin:** Writing – review & editing, Methodology, Investigation, Data curation, Conceptualization. **Yuheng Shang:** Writing – review & editing, Formal analysis. **Robert Lovšin:** Investigation, Formal analysis. **Nina Kovač:** Writing – review & editing, Investigation. **Samo Jereb:** Writing – original draft, Visualization, Software, Formal analysis, Data curation. **Armin Hadžić:** Writing – original draft, Data curation. **Matevž Zupančič:** Writing – original draft, Resources, Formal analysis. **Maria Rosaria Vetrano:** Writing – review & editing, Supervision, Resources, Project administration, Funding acquisition. **Iztok Golobič:** Writing – review & editing, Supervision, Resources, Project administration, Funding acquisition.

Declaration of competing interest

The authors declare that they have no known competing financial interests or personal relationships that could have appeared to influence the work reported in this paper.

Acknowledgements

The authors acknowledge financial support from the Slovenian Research And Innovation Agency (research core funding No P2–0223 and P1–0134, and project No J2–50085). The authors acknowledge financial support from the China Scholarship Council (Grant No. 202106280059). Dr. Gustav Graeber (Humboldt-Universität zu Berlin) is thanked for his insight into the exploration of cascade freezing. The authors acknowledge Barbara Kapun (Jožef Stefan Institute) for performing the SEM/EDS analysis.

References

[1] S. Zhang, J. Huang, Y. Cheng, H. Yang, Z. Chen, Y. Lai, Bioinspired surfaces with superwettability for anti-icing and ice-phobic application: concept, mechanism, and design, Small 13 (2017) 1–20, https://doi.org/10.1002/smll.201701867.
[2] Y. Lin, H. Chen, G. Wang, A. Liu, Recent progress in preparation and anti-icing applications of superhydrophobic coatings, Coatings 8 (2018), https://doi.org/10.3390/coatings8060208.
[3] W. Li, Y. Zhan, S. Yu, Applications of superhydrophobic coatings in anti-icing: theory, mechanisms, impact factors, challenges and perspectives, Prog. Org. Coatings 152 (2021) 106117, https://doi.org/10.1016/j.porgcoat.2020.106117.
[4] E. Vazirinasab, R. Jafari, G. Momen, Application of superhydrophobic coatings as a corrosion barrier: a review, Surf. Coatings Technol. 341 (2018) 40–56, https://doi.org/10.1016/j.surfcoat.2017.11.053.
[5] A.M.A. Mohamed, A.M. Abdullah, N.A. Younan, Corrosion behavior of superhydrophobic surfaces: a review, Arab. J. Chem. 8 (2015) 749–765, https://doi.org/10.1016/j.arabjc.2014.03.006.
[6] A.A. Farag, E.A. Mohamed, A. Toghan, The new trends in corrosion control using superhydrophobic surfaces: a review, Corros. Rev. 41 (2023) 21–37, https://doi.org/10.1515/corrrev-2022-0020.
[7] A. Samanta, Q. Wang, S.K. Shaw, H. Ding, Roles of chemistry modification for laser textured metal alloys to achieve extreme surface wetting behaviors, Mater. Des. 192 (2020) 108744, https://doi.org/10.1016/j.matdes.2020.108744.
[8] H. Sojoudi, G.H. McKinley, K.K. Gleason, Linker-free grafting of fluorinated polymeric cross-linked network bilayers for durable reduction of ice adhesion, Mater. Horizons 2 (2015) 91–99, https://doi.org/10.1039/c4mh00162a.
[9] M. Susoff, K. Siegmann, C. Pfaffenroth, M. Hirayama, Evaluation of icephobic coatings - screening of different coatings and influence of roughness, Appl. Surf. Sci. 282 (2013) 870–879, https://doi.org/10.1016/j.apsusc.2013.06.073.
[10] G. Wang, Z. Guo, Liquid infused surfaces with anti-icing properties, Nanoscale 11 (2019) 22615–22635, https://doi.org/10.1039/c9nr06934h.
[11] S. Heydarian, R. Jafari, G. Momen, Recent progress in the anti-icing performance of slippery liquid-infused surfaces, Prog. Org. Coatings 151 (2021) 106096, https://doi.org/10.1016/j.porgcoat.2020.106096.
[12] P. Tourkine, M. Le Merrer, D. Quéré, Delayed freezing on water repellent materials, Langmuir 25 (2009) 7214–7216, https://doi.org/10.1021/la900929u.
[13] T. Maitra, C. Antonini, M.K. Tiwari, A. Mularczyk, Z. Imeri, P. Schoch, D. Poulikakos, Supercooled water drops impacting superhydrophobic textures, Langmuir 30 (2014) 10855–10861, https://doi.org/10.1021/la502675a.
[14] Q. Wang, A. Chen, H. Gu, G. Qin, J. Zhang, J. Xu, G. Jiang, W. Liu, Z. Zhang, H. Huang, Highly interconnected porous PDMS/CNTs sandwich sponges with anti-icing/deicing microstructured surfaces, J. Mater. Sci. 56 (2021) 11723–11735, https://doi.org/10.1007/s10853-021-06052-4.
[15] Y. Shen, X. Xie, Y. Xie, J. Tao, J. Jiang, H. Chen, Y. Lu, Y. Xu, Statistically understanding the roles of nanostructure features in interfacial ice nucleation for enhancing icing delay performance, Phys. Chem. Chem. Phys. 21 (2019) 19785–19794, https://doi.org/10.1039/c9cp04103f.
[16] J.B. Boreyko, B.R. Srijanto, T.D. Nguyen, C. Vega, M. Fuentes-Cabrera, C.P. Collier, Dynamic defrosting on nanostructured superhydrophobic surfaces, Langmuir 29 (2013) 9516–9524, https://doi.org/10.1021/la401282c.
[17] Y. Jian, H. Gao, Y. Yan, Fabrication of a superhydrophobic micron-nanoscale hierarchical structured surface for delayed icing and reduced frosting, surfaces and interfaces, Surf. Interface 34 (2022) 102353, https://doi.org/10.1016/j.surfin.2022.102353.

[18] C. Wu, H. Geng, S. Tan, J. Lv, H. Wang, Z. He, J. Wang, Highly efficient solar anti-icing/deicing: via a hierarchical structured surface, Mater. Horizons. 7 (2020) 2097–2104, https://doi.org/10.1039/d0mh00636j.

[19] G. He, S. Lu, W. Xu, J. Yu, B. Wu, S. Cui, Fabrication of durable superhydrophobic electrodeposited tin surfaces with tremella-like structure on copper substrate, Surf. Coatings Technol. 309 (2017) 590–599, https://doi.org/10.1016/j.surfcoat.2016.12.014.

[20] Y. Li, S. Dai, J. John, K.R. Carter, Superhydrophobic surfaces from hierarchically structured wrinkled polymers, ACS Appl. Mater. Interfaces 5 (2013) 11066–11073, https://doi.org/10.1021/am403209r.

[21] P. Rodič, I. Milošev, One-step ultrasound fabrication of corrosion resistant, self-cleaning and anti-icing coatings on aluminium, Surf. Coatings Technol. 369 (2019) 175–185, https://doi.org/10.1016/j.surfcoat.2019.03.082.

[22] I. Milošev, T. Bakarič, S. Zanna, A. Seyeux, P. Rodič, M. Poberžnik, F. Chiter, P. Cornette, D. Costa, A. Kokalj, P. Marcus, Electrochemical, surface-analytical, and computational DFT study of alkaline etched aluminum modified by carboxylic acids for corrosion protection and hydrophobicity, J. Electrochem. Soc. 166 (2019) C3131–C3146, https://doi.org/10.1149/2.0181911jes.

[23] P. Rodič, B. Kapun, I. Milošev, Superhydrophobic aluminium surface to enhance corrosion resistance and obtain self-cleaning and anti-icing ability, Molecules 27 (2022) 1099, https://doi.org/10.3390/molecules27031099.

[24] P. Rodič, B. Kapun, M. Panjan, I. Milošev, Easy and fast fabrication of self-cleaning and anti-icing perfluoroalkyl silane film on aluminium, Coatings 10 (2020) 234, https://doi.org/10.3390/coatings10030234.

[25] C. Zhang, C. Li, Z. He, D. Gao, J. Qi, J. Cao, The fabrication of unwettable superhydrophobic surfaces by reactive wetting of AgCuTi into an AAO template, Appl. Surf. Sci. 604 (2022), https://doi.org/10.1016/j.apsusc.2022.154499.

[26] N. Celik, I. Torun, M. Ruzi, A. Esidir, M.S. Onses, Fabrication of robust superhydrophobic surfaces by one-step spray coating: evaporation driven self-assembly of wax and nanoparticles into hierarchical structures, Chem. Eng. J. 396 (2020), https://doi.org/10.1016/j.cej.2020.125230.

[27] G. Yu, G. Jiang, Fabrication of a superhydrophobic surface with photothermal electrical conversion performance for anti-icing, Surf. Interfaces (Provid.) 46 (2024) 104089, https://doi.org/10.1016/j.surfin.2024.104089.

[28] M. Može, M. Senegačnik, P. Gregorčič, M. Hočevar, M. Zupančič, I. Golobič, Laser-engineered microcavity surfaces with a nanoscale superhydrophobic coating for extreme boiling performance, ACS Appl. Mater. Interfaces (Provid.) 12 (2020) 24419–24431, https://doi.org/10.1021/acsami.0c01594.

[29] A. Hadžić, M. Može, M. Zupančič, I. Golobič, Superbiphilic laser-microengineered surfaces with a self-assembled monolayer coating for exceptional boiling performance, Adv. Funct. Mater. (2023), https://doi.org/10.1002/adfm.202310662.

[30] C. Ge, G. Yuan, C. Guo, C.V. Ngo, W. Li, Femtosecond laser fabrication of square pillars integrated Siberian-Cocklebur-like microstructures surface for anti-icing, Mater. Des. 204 (2021), https://doi.org/10.1016/j.matdes.2021.109689.

[31] S. Alamri, V. Vercillo, A.I. Aguilar-Morales, F. Schell, M. Wetterwald, A.F. Lasagni, E. Bonaccurso, T. Kunze, Self-limited ice formation and efficient de-icing on superhydrophobic micro-structured airfoils through direct laser interference patterning, Adv. Mater. Interfaces 7 (2020), https://doi.org/10.1002/admi.202001231.

[32] J. Li, Y. Zhou, W. Wang, C. Xu, L. Ren, Superhydrophobic copper surface textured by laser for delayed icing phenomenon, Langmuir 36 (2020) 1075–1082, https://doi.org/10.1021/acs.langmuir.9b02273.

[33] Y. Wan, C. Yan, H. Yu, B. Wang, Anti-icing performance of superhydrophobic surface with square-ring structure prepared by nanosecond laser, Adv. Eng. Mater. 23 (2021), https://doi.org/10.1002/adem.202100190.

[34] U. Trdan, M. Hočevar, P. Gregorčič, Transition from superhydrophilic to superhydrophobic state of laser textured stainless steel surface and its effect on corrosion resistance, Corros. Sci. 123 (2017) 21–26, https://doi.org/10.1016/j.corsci.2017.04.005.

[35] M. Conradi, T. Sever, P. Gregorčič, A. Kocijan, Short- and long-term wettability evolution and corrosion resistance of uncoated and polymer-coated laser-textured steel surface, Coatings 9 (2019) 592, https://doi.org/10.3390/coatings9090592.

[36] L. Zhang, Z. Tan, C. Zhang, J. Tang, C. Yao, X. You, B. Hao, Research on metal corrosion resistant bioinspired special wetting surface based on laser texturing technology: a review, Micromachines 13 (2022), https://doi.org/10.3390/mi13091431.

[37] Q. Ma, Z. Tong, W. Wang, G. Dong, Fabricating robust and repairable superhydrophobic surface on carbon steel by nanosecond laser texturing for corrosion protection, Appl. Surf. Sci. 455 (2018) 748–757, https://doi.org/10.1016/j.apsusc.2018.06.033.

[38] S.J. Caraguay, T.S. Pereira, R.O. Giacomelli, A. Cunha, M. Pereira, F.A. Xavier, The effect of laser surface textures on the corrosion resistance of epoxy coated steel exposed to aggressive environments for offshore applications, Surf. Coatings Technol. 437 (2022), https://doi.org/10.1016/j.surfcoat.2022.128371.

[39] J.I. Ahuir-Torres, M.A. Arenas, W. Perrie, G. Dearden, J. de Damborenea, Surface texturing of aluminium alloy AA2024-T3 by picosecond laser: effect on wettability and corrosion properties, Surf. Coatings Technol. 321 (2017) 279–291, https://doi.org/10.1016/j.surfcoat.2017.04.056.

[40] G.U. Kumar, S. Suresh, C.S. Sujith Kumar, S. Back, B. Kang, H.J. Lee, A review on the role of laser textured surfaces on boiling heat transfer, Appl. Therm. Eng. 174 (2020) 115274, https://doi.org/10.1016/j.applthermaleng.2020.115274.

[41] V. Serdyukov, S. Starinskiy, I. Malakhov, A. Safonov, A. Surtaev, Laser texturing of silicon surface to enhance nucleate pool boiling heat transfer, Appl. Therm. Eng. 194 (2021), https://doi.org/10.1016/j.applthermaleng.2021.117102.

[42] C.M. Kruse, T. Anderson, C. Wilson, C. Zuhlke, D. Alexander, G. Gogos, S. Ndao, Enhanced pool-boiling heat transfer and critical heat flux on femtosecond laser processed stainless steel surfaces, Int. J. Heat Mass Transf. 82 (2015) 109–116, https://doi.org/10.1016/j.ijheatmasstransfer.2014.11.023.

[43] D. Žalec, M. Može, M. Zupančič, I. Golobič, Elucidating the effects of surface wettability on boiling heat transfer using hydrophilic and hydrophobic surfaces with laser-etched microchannels, Case Stud. Therm. Eng. 57 (2024), https://doi.org/10.1016/j.csite.2024.104357.

[44] D. Patil, S. Aravindan, R. Sarathi, P.V. Rao, Fabrication of self-cleaning superhydrophobic silicone rubber insulator through laser texturing, Surf. Eng. 37 (2021) 308–317, https://doi.org/10.1080/02670844.2020.1780673.

[45] H. Wang, Q. Wang, L. Huo, J. Liu, Z. Bai, High-efficient laser-based bionic surface structuring for enhanced surface functionalization and self-cleaning effect, Surf. Interfaces (Provid.) 37 (2023), https://doi.org/10.1016/j.surfin.2023.102691.

[46] S. Milles, M. Soldera, T. Kuntze, A.F. Lasagni, Characterization of self-cleaning properties on superhydrophobic aluminum surfaces fabricated by direct laser writing and direct laser interference patterning, Appl. Surf. Sci. 525 (2020), https://doi.org/10.1016/j.apsusc.2020.146518.

[47] S.C. Vanithakumari, C. Ambar Kumar, C. Thinaharan, G. Ram Kishor, R.P. George, R. Kaul, K.S. Bindra, P. John, Laser patterned titanium surfaces with superior antibiofouling, superhydrophobicity, self-cleaning and durability: role of line spacing, Surf. Coatings Technol. 418 (2021), https://doi.org/10.1016/j.surfcoat.2021.127257.

[48] P. Rodič, N. Kovač, S. Kralj, S. Jereb, I. Golobič, M. Može, I. Milošev, Anti-corrosion and anti-icing properties of superhydrophobic laser-textured aluminum surfaces, Surf. Coatings Technol. 494 (2024) 131325, https://doi.org/10.1016/j.surfcoat.2024.131325.

[49] N. Kovač, M. Može, B. Kapun, I. Golobič, I. Milošev, P. Rodič, Enhanced corrosion resistance and self-cleaning of AlSi7Mg0.3 via superhydrophobic surface using laser structuring and stearic acid grafting, Surf. Interfaces (Provid.) 61 (2025) 106089, https://doi.org/10.1016/j.surfin.2025.106089.

[50] J. Schille, L. Schneider, S. Mauersberger, S. Szokup, S. Höhn, J. Pötschke, F. Reiß, E. Leidich, U. Löschner, High-rate laser surface texturing for advanced tribological functionality, Lubricants 8 (2020), https://doi.org/10.3390/lubricants8030033.

[51] S. Liu, Q. Sai, S. Wang, J. Williams, Effects of laser surface texturing and lubrication on the vibrational and tribological performance of sliding contact, Lubricants 10 (2022), https://doi.org/10.3390/lubricants10010010.

[52] N. Radek, D. Tokar, A. Kalinowski, J. Pietraszek, Influence of laser texturing on tribological properties of DLC coatings, Prod. Eng. Arch. 27 (2021) 119–123, https://doi.org/10.30657/pea.2021.27.15.

[53] A. Woźniak, O. Bialas, M. Adamiak, B. Hadzima, J. Szewczenko, The influence of laser texturing on the tribological behavior of titanium alloy Ti6Al4V in medical applications, Arch. Civ. Mech. Eng. 24 (2024), https://doi.org/10.1007/s43452-024-00960-3.

[54] A. Singh, D.S. Patel, J. Ramkumar, K. Balani, Single step laser surface texturing for enhancing contact angle and tribological properties, Int. J. Adv. Manuf. Technol. 100 (2019) 1253–1267, https://doi.org/10.1007/s00170-018-1579-8.

[55] D. Maldonado-Cortés, L. Peña-Parás, N.R. Martínez, M.P. Leal, D.I. Quintanilla Correa, Tribological characterization of different geometries generated with laser surface texturing for tooling applications, Wear 477 (2021), https://doi.org/10.1016/j.wear.2021.203856.

[56] Y. Wang, Y. Sun, Y. Xue, F. Wang, W. Liang, Y. Wang, D. Zhu, H. Zhao, Near-infrared light-responsive functionalised surfaces with shape memory microstructure for droplet manipulation and anti-icing/de-icing, Surf. Interfaces (Provid.) 40 (2023) 103056, https://doi.org/10.1016/j.surfin.2023.103056.

[57] V. Vercillo, J.T. Cardoso, D. Huerta-Murillo, S. Tonnicchia, A. Laroche, J.A. Mayén Guillén, J.L. Ocaña, A.F. Lasagni, E. Bonaccurso, Durability of superhydrophobic laser-treated metal surfaces under icing conditions, Mater. Lett. X. 3 (2019) 100021, https://doi.org/10.1016/j.mlblux.2019.100021.

[58] V.J. Rico, C. López-Santos, M. Villagrá, J.P. Espinós, G.F. De La Fuente, L. A. Angurel, A. Borrás, A.R. González-Elipe, Hydrophobicity, freezing delay, and morphology of laser-treated aluminum surfaces, Langmuir 35 (2019) 6483–6491, https://doi.org/10.1021/acs.langmuir.9b00457.

[59] A. Volpe, C. Gaudiuso, L. Di Venere, F. Licciulli, F. Giordano, A. Ancona, Direct femtosecond laser fabrication of superhydrophobic aluminum alloy surfaces with anti-icing properties, Coatings 10 (2020), https://doi.org/10.3390/COATINGS10060587.

[60] Y. Wang, Y. Xue, Y. Sun, X. Sui, Y. Wang, W. Liang, Y. Wang, D. Zhu, H. Zhao, Flexible superhydrophobic films with the electrothermal and photothermal response for enhanced passive anti-icing and active de-icing, Surf. Interfaces (Provid.) 42 (2023) 103430, https://doi.org/10.1016/j.surfin.2023.103430.

[61] L. Wang, H. Zhao, D. Zhu, L. Yuan, H. Zhang, P. Fan, M. Zhong, A review on ultrafast laser enabled excellent superhydrophobic anti-icing performances, Appl. Sci. 13 (2023), https://doi.org/10.3390/app13095478.

[62] S. Milles, V. Vercillo, S. Alamri, A.I. Aguilar-Morales, T. Kunze, E. Bonaccurso, A. F. Lasagni, Icephobic performance of multi-scale laser-textured aluminum surfaces for aeronautic applications, Nanomaterials 11 (2021) 1–17, https://doi.org/10.3390/nano11010135.

[63] J. Zheng, R. Liu, D. Liu, Z. Weng, G. Song, W. Li, Z. Wang, Slippery liquid infused porous surfaces with anti-icing performance fabricated by direct laser interference lithography, Prog. Org. Coatings 175 (2023) 107308, https://doi.org/10.1016/j.porgcoat.2022.107308.

[64] L.B. Boinovich, K.A. Emelyanenko, A.M. Emelyanenko, Superhydrophobic *versus* SLIPS: temperature dependence and the stability of ice adhesion strength, J. Colloid Interface Sci. 606 (2022) 556–566, https://doi.org/10.1016/j.jcis.2021.08.030.

[65] Z. Liu, F. Ye, H. Tao, J. Lin, Effects of frost formation on the ice adhesion of micro-nano structure metal surface by femtosecond laser, J. Colloid Interface Sci. 603 (2021) 233–242, https://doi.org/10.1016/j.jcis.2021.06.105.
[66] Z. Liu, H. Tao, J. Lin, Anisotropic ice adhesion of micro-nano-structured metal surface by a femtosecond laser, Langmuir 37 (2021) 9571–9576, https://doi.org/10.1021/acs.langmuir.1c01459.
[67] L. Montes, V. Rico, F. Nuñez-Galvez, M.Á. Arenas, A.C. del Campo, V. Lopez-Flores, J.P. Espinós, A. Borrás, A.R. González-Elipe, C. López-Santos, Long-lasting low fluorinated stainless steel hierarchical surfaces for omniphobic, anti-fouling and anti-icing applications, Surf. Interfaces (Provid.) 46 (2024), https://doi.org/10.1016/j.surfin.2024.104167.
[68] X. Li, H. Su, H. Li, X. Tan, X. Lin, Y. Wu, X. Xiong, Z. Li, L. Jiang, T. Xiao, W. Chen, X. Tan, Photothermal superhydrophobic surface with good corrosion resistance, anti-/de-icing property and mechanical robustness fabricated via multiple-pulse laser ablation, Appl. Surf. Sci. 646 (2024) 158944, https://doi.org/10.1016/j.apsusc.2023.158944.
[69] M. Cui, H. Huang, H. Wu, L. Zhang, J. Yan, Achieving superhydrophobicity of Zr-based metallic glass surface with anti-corrosion and anti-icing properties by nanosecond laser ablation and subsequent heat treatment, Surf. Coatings Technol. 475 (2023) 130159, https://doi.org/10.1016/j.surfcoat.2023.130159.
[70] Y. Shu, X. Lu, W. Lu, W. Su, Y. Wu, H. Wei, D. Xu, J. Liang, Y. Xie, Mechanically robust superhydrophobic copper surface with self-cleaning, anti-icing, and corrosion resistance, Surf. Coatings Technol. 455 (2023) 129216, https://doi.org/10.1016/j.surfcoat.2022.129216.
[71] X. Wan, I. Lieberman, A. Asyuda, S. Resch, H. Seim, P. Kirsch, M. Zharnikov, Thermal stability of phosphonic acid self-assembled monolayers on alumina substrates, J. Phys. Chem. C. 124 (2020) 2531–2542, https://doi.org/10.1021/acs.jpcc.9b10628.
[72] D. Žalec, A. Hadžić, M. Može, I. Golobič, Hierarchical surfaces with open microchannels and laser-induced microcavities for enhancement of pool boiling critical heat flux, Int. J. Heat Mass Transf. 235 (2024) 126192, https://doi.org/10.1016/j.ijheatmasstransfer.2024.126192.
[73] K. Nakayama, A. Koyama, C. Zhu, Y. Aoki, H. Habazaki, Rapid and repeatable self-healing superoleophobic porous aluminum surface using infiltrated liquid healing agent, Adv. Mater. Interfaces 5 (2018), https://doi.org/10.1002/admi.201800566.
[74] M. Wang, I.G. Hill, Fluorinated alkyl phosphonic acid SAMs replace PEDOT:PSS in polymer semiconductor devices, Org. Electron. 13 (2012) 498–505, https://doi.org/10.1016/j.orgel.2011.12.008.
[75] J. Berce, A. Hadžić, M. Može, K. Arhar, H. Gjerkeš, M. Zupančič, I. Golobič, Effect of surface wettability on nanoparticle deposition during pool boiling on laser-textured copper surfaces, Nanomaterials 14 (2024), https://doi.org/10.3390/nano14030311.
[76] T. Shirai, S. Yamauchi, H. Kikuchi, H. Fukumoto, H. Tsukada, T. Agou, Synthesis, characterization, and formation of self-assembled monolayers of a phosphonic acid bearing a vinylene-bridged fluoroalkyl chain, Appl. Surf. Sci. 577 (2022), https://doi.org/10.1016/j.apsusc.2021.151959.
[77] J. Berce, K. Arhar, A. Hadžić, M. Zupančič, M. Može, I. Golobič, Boiling-induced surface aging and crystallization fouling of functionalized smooth and laser-textured copper interfaces, Appl. Therm. Eng. 242 (2024), https://doi.org/10.1016/j.applthermaleng.2024.122540.
[78] B. Bhushan, M. Cichomski, E. Hoque, J.A. Derose, P. Hoffmann, H.J. Mathieu, Nanotribological characterization of perfluoroalkylphosphonate self-assembled monolayers deposited on aluminum-coated silicon substrates, Microsyst. Technol. 12 (2006) 588–596, https://doi.org/10.1007/s00542-006-0111-5.
[79] L. Stendardo, G. Gastaldo, M. Budinger, V. Pommier-Budinger, I. Tagliaro, P. F. Ibáñez-Ibáñez, C. Antonini, Reframing ice adhesion mechanisms on a solid surface, Appl. Surf. Sci. 641 (2023), https://doi.org/10.1016/j.apsusc.2023.158462.
[80] M. Poberžnik, D. Costa, A. Hemeryck, A. Kokalj, Insight into the bonding of silanols to oxidized aluminum surfaces, J. Phys. Chem. C. 122 (2018) 9417–9431, https://doi.org/10.1021/acs.jpcc.7b12552.
[81] I. Milošev, D. Zimerl, C. Carriére, S. Zanna, A. Seyeux, J. Iskra, S. Stavber, F. Chiter, M. Poberžnik, D. Costa, A. Kokalj, P. Marcus, The effect of anchor group and alkyl backbone chain on performance of organic compounds as corrosion inhibitors for aluminum investigated using an integrative experimental-modeling approach, J. Electrochem. Soc. 167 (2020) 061509, https://doi.org/10.1149/1945-7111/ab829d.
[82] J. Sebilleau, E. Ablonet, P. Tordjeman, D. Legendre, Air humidity effects on water-drop icing, Phys. Rev. E. 104 (2021) 1–7, https://doi.org/10.1103/PhysRevE.104.L032802.
[83] K. Maghsoudi, G. Momen, R. Jafari, M. Farzaneh, Direct replication of micro-nanostructures in the fabrication of superhydrophobic silicone rubber surfaces by compression molding, Appl. Surf. Sci. 458 (2018) 619–628, https://doi.org/10.1016/j.apsusc.2018.07.099.
[84] C. Guo, M. Zhang, J. Hu, Icing delay of sessile water droplets on superhydrophobic titanium alloy surfaces, Colloids Surf. A Physicochem. Eng. Asp. 621 (2021) 126587, https://doi.org/10.1016/j.colsurfa.2021.126587.
[85] J.L. McCormick, J.W. Westwater, Nucleation sites for dropwise condensation, Chem. Eng. Sci. 20 (1965) 1021–1036, https://doi.org/10.1016/0009-2509(65)80104-X.
[86] S. Jung, M.K. Tiwari, D. Poulikakos, Frost halos from supercooled water droplets, Proc. Natl. Acad. Sci. U. S. A. 109 (2012) 16073–16078, https://doi.org/10.1073/pnas.1206121109.
[87] G. Graeber, V. Dolder, T.M. Schutzius, D. Poulikakos, Cascade freezing of supercooled water droplet collectives, ACS Nano 12 (2018) 11274–11281, https://doi.org/10.1021/acsnano.8b05921.
[88] Y. Zhao, R. Wang, C. Yang, Interdroplet freezing wave propagation of condensation frosting on micropillar patterned superhydrophobic surfaces of varying pitches, Int. J. Heat Mass Transf. 108 (2017) 1048–1056, https://doi.org/10.1016/j.ijheatmasstransfer.2016.12.112.
[89] J.B. Boreyko, R.R. Hansen, K.R. Murphy, S. Nath, S.T. Retterer, C.P. Collier, Controlling condensation and frost growth with chemical micropatterns, Sci. Rep. 6 (2016) 1–15, https://doi.org/10.1038/srep19131.
[90] N.H. Fletcher, Size effect in heterogeneous nucleation, J. Chem. Phys. 29 (1958) 572–576, https://doi.org/10.1063/1.1744540.
[91] S. Jung, M.K. Tiwari, N.V. Doan, D. Poulikakos, Mechanism of supercooled droplet freezing on surfaces, Nat. Commun. 3 (2012), https://doi.org/10.1038/ncomms1630.
[92] O. Seri, The effect of NaCl concentration on the corrosion behavior of aluminum containing iron, Corros. Sci. 36 (1994) 1789–1803, https://doi.org/10.1016/0010-938X(94)90132-5.
[93] J.R. Davis, Corrosion of aluminum and aluminum alloys, 1999.
[94] C.-V. Ngo, D.-M. Chun, Control of laser-ablated aluminum surface wettability to superhydrophobic or superhydrophilic through simple heat treatment or water boiling post-processing, Appl. Surf. Sci. 435 (2018) 974–982, https://doi.org/10.1016/j.apsusc.2017.11.185.
[95] R. Zhao, P. Rupper, S. Gaan, Recent development in phosphonic acid-based organic coatings on aluminum, Coatings 7 (2017) 133, https://doi.org/10.3390/coatings7090133.
[96] R. Zhao, R. Hauert, R. Crockett, C. Cancellieri, S. Gaan, P. Schmutz, M. Heuberger, L.P.H. Jeurgens, Aqueous phosphonic acid treatments of aluminium: effect of oxide dissolution and re-oxidation on adsorbate formation, Appl. Surf. Sci. 667 (2024) 160363, https://doi.org/10.1016/j.apsusc.2024.160363.